Morphodynamics of bedforms in a supercritical-flow regime: a depth-resolved numerical modelling approach

Age J. Vellinga

M.Sc. Thesis Earth Sciences, Utrecht University

Supervisors: Dr. Joris T. Eggenhuisen and Dr. Matthieu J.B. Cartigny

August 2014

Abstract

Both open-channel flows and density currents are able to create supercritical-flow bedforms. The morphodynamics of these supercritical-flow bedforms are, however, still poorly understood. This is mainly due to a lack of measurements of flow processes occurring within these types of flows. Cyclic steps have successfully been simulated in open-channel flow using a depth-resolved numerical model. The equilibrium conditions at which certain supercritical-flow bedforms are stable are investigated. The temporal variation in Froude number is indicative of at which conditions cyclic steps are in a macroscopic equilibrium at a variability of grain sizes, discharges and sediment concentrations. The depth-resolved model provides insight into the dynamic interaction between velocity structure, shear stresses, and sediment concentrations within the flows and resulting erosion and deposition patterns, which, in their turn affect the flow-properties again. The velocity structure downstream of a hydraulic jump displays highest flow velocities near the bed, whilst lowest or even negative velocities are located at the top of the flow, causing the flow to remain exerting shear stresses on the bed even after the hydraulic jump. The sediment concentrations within the flow only decrease after a 30 second, or half a meter lag, causing most of the deposition to take place at the last two-thirds of subcritical region of the flow. The resulting depositional pattern consists of upstream-dipping backset laminations deposited on the stoss-side of the bedform, cross-cut by the erosive surface of the lee-side of the cyclic step, this interplay between erosion and deposition also causes an upstream migration of the cyclic steps.

Introduction

Unidirectional fluid flow over an erodible bed usually leads to the formation of bedforms due to the morphodynamic interaction of a flow and a sedimentary bed, such bedforms have been observed in both open-channel flows as well as in density currents. Two main types of bedforms can also be created by an overall supercritical-flow; antidunes and cyclic steps. Supercritical-flow bedforms have been modelled in flume experiments in both open-channel as well as density flows (Jorritsma, 1973; Taki & Parker, 2004; Alexander et al., 2010; Spinewine et al., 2009; Cartigny et al., 2013). Additionally there are field observations of these bedforms in free-surface flows (Simons et al., 1965; Grand, 1997; Fielding, 2006). Bedforms with similar geometries and internal structures have also been

observed on the seafloor (Smith, 2005; Lamb et al., 2006; Fildani et al., 2006; Heiniö & Davies, 2009; Paull et al., 2010; Ayranci et al., 2012; Hughes-Clarke et al., 2012), though the interpretation of the process creating these sediment waves is debated. Numerical modelling studies on supercritical bedforms have been performed, using depth-averaged models, both in open-channel setting (Winterwerp et al., 1992; Parker & Izumi, 2000; Mastbergen & Van Den Berg, 2003; Fagherazzi & Sun, 2003; Parker & Sun, 2005) and under subaqueous conditions (Fildani et al., 2006; Kostic & Parker, 2006; Kostic et al., 2010; Cartigny et al., 2011; Covault et al., 2014).

These depth-averaged models have provided valuable insights in the morphodynamics of bedform development. The fundamental instability underlying the initiation of bedforms, as well as the dynamic flow processes associated with them, are however, still poorly constrained. The simplification in internal flow structure limits information on bed-flow interaction that can be extracted from the depth-averaged models. Differences in sediment concentration, turbulence and velocity may affect the bed interaction significantly.

More detailed numerical simulations of the flow-processes and bed-flow interactions allow a more detailed constrain of the parameters governing the formation of bedforms; data which is difficult to obtain from the actual natural flows or physical experiments. In this study a fully depth-resolved computational fluid dynamics (CFD) commercial code that uses a Reynolds-averaged Navier-Stokes approach (RANS) is deployed in order to gain further insights in the processes forming and maintaining the supercritical-flow bedforms over time, at different conditions.

The main research questions of this study are: (1) can supercritical bedforms be modelled using a depth-resolved model? This type of numerical algorithm has never been used to simulate the development of supercritical-flow bedforms, the model outcomes are first to be compared to physical modelling results to validate the use of the model. (2) At which conditions do supercritical bedforms develop from an initially smooth slope? The effects of grain size, specific discharge and sediment concentration on flow conditions will be investigated. (3) How does the morphodynamic interaction between flow and bedform work? How does the bed-morphology affect the flow-properties? The model allows for quantification of flow-properties as excess-shear stress, sediment concentration and flow-velocity over depth. (4) An attempted has been made to model supercritical-flow bedforms in a turbidity current, with the experimental work of Jorritsma (1973) as a basis. Although stable conditions under which supercritical bedforms have been formed have proven difficult to model, the bed-flow interaction has been simulated. The effects of different physical flow properties on the bed and vice-versa around a hydraulic jump in a turbidity current will be investigated.

Background

Flows are either Froude subcritical (Fr<1) or supercritical (Fr>1), as a flow shifts from a supercritical - to a subcritical flow regime, a hydraulic jump is present. This fluid-dynamic process can be observed in free-surface conditions as well as in turbidity currents (Komar, 1971; Long et al., 1990; Hager, 1992; Kostic et al., 2010). In supercritical flow conditions there are two main types of bedforms that can be present (Kennedy, 1960; Alexander et al., 2001; Cartigny et al., 2013) (1) Antidunes: antidunes are short wavelength, relative to cyclic-steps, symmetrical bedforms associated with continuously supercritical flow and (2) Cyclic steps: cyclic steps are generally more asymmetrical, longer wavelength bedforms, associated with trains of hydraulic jumps. On the stoss-side of the cyclic step, depositional subcritical flow is present, while at the lee-side there is an erosive supercritical flow (Winterwerp et al., 1992; Parker, 1996; Cartigny et al., 2013 There are also two transitional bedforms related to Froude-supercritical flow: unstable antidunes and chutes-and-pools (Kennedy, 1960; Kennedy, 1961; Alexander et al., 2001; Cartigny et al., 2013), an overview of the different supercritical-flow bedforms is shown in figure 1.

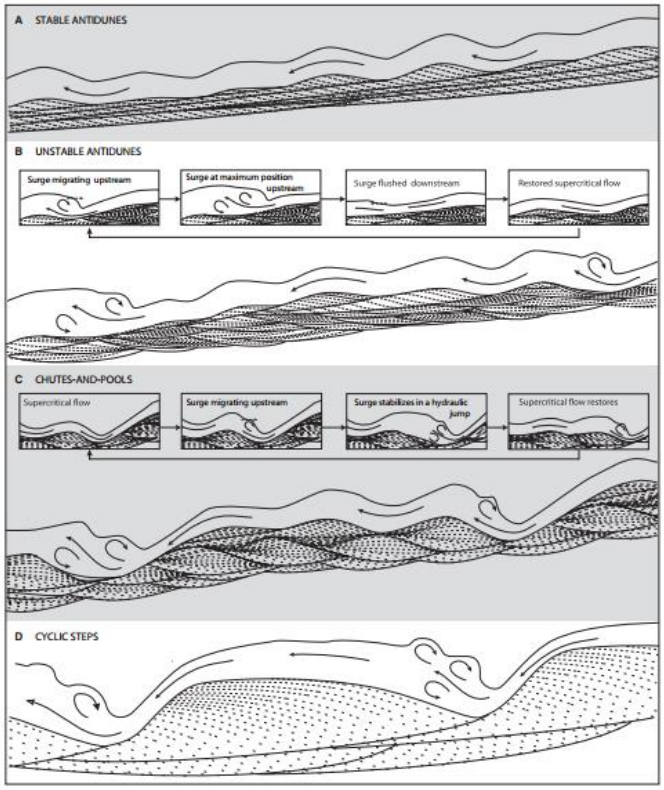

Figure 1: An illustration of different kinds of supercritical bedforms as found in Cartigny et al., (2013).

Fluid-dynamic framework

Flow regimes and hydraulic jumps

The Froude number is an important number in hydrodynamics, as the Froude number distinguishes between subcritical flows where surface waves can migrate both upstream and downstream, and supercritical flows which only allow downstream migration of surface waves. The Froude number (Fr) is the dimensionless ratio between flow velocity and wave propagation velocity, but it also represents the ratio between the flow's inertia and gravitational forces when applied to depth-average flow properties.

$$Fr = \frac{u}{\sqrt{gh}} \qquad \text{Equation 1.1}$$

In which u is the depth-averaged flow velocity, g the acceleration due to gravity and h the flow depth. If Fr>1 the flow is supercritical, and if Fr<1 the flow is deemed subcritical.

The transition between supercritical to subcritical-flow is associated with the formation of hydraulic jumps, which can be explained in terms of specific energy. The specific energy is the sum of kinetic energy ($\frac{1}{2}\rho u^2$) and potential energy (ρgh), where ρ is the density of the fluid. The specific energy can be expressed in meters of water column height by dividing by ρg. Assuming uniform density and velocity distributions this results in equation 1.2. The specific energy (E) is expressed in metres of

water column, in which the first term corresponds with the potential energy head (E_s), and the second with the kinetic energy head (E_k), q is the specific discharge.

$$E = E_s + E_k \propto \rho g h + \frac{1}{2}\rho u^2 \propto h + \frac{u^2}{2g} = h + \frac{q^2}{2gh^2} \qquad \text{Equation 1.2}$$

This function implies that the energy in a flow is the sum of the kinetic energy and potential energy. As the Froude number (equation 1.1) is a ratio between the fluids inertia and gravitational forces, it can be said that the square of the Froude number is proportional to the kinetic and potential energy (equation 1.3). This also means that there is a critical flow velocity (u_c) and critical flow depth (h_c) (at constant discharge), at which the flow changes from a supercritical to subcritical flow regime (and vice versa),

$$\frac{kinetic}{potential} = \frac{½\rho u^2}{\rho g h} = \frac{u^2}{2gh} \propto Fr^2 \qquad \text{Equation 1.3}$$

The critical flow depth can be used to non-dimensionalise the flow depth (h/h_c), and specific energy expressed in hydraulic head (E/h_c).

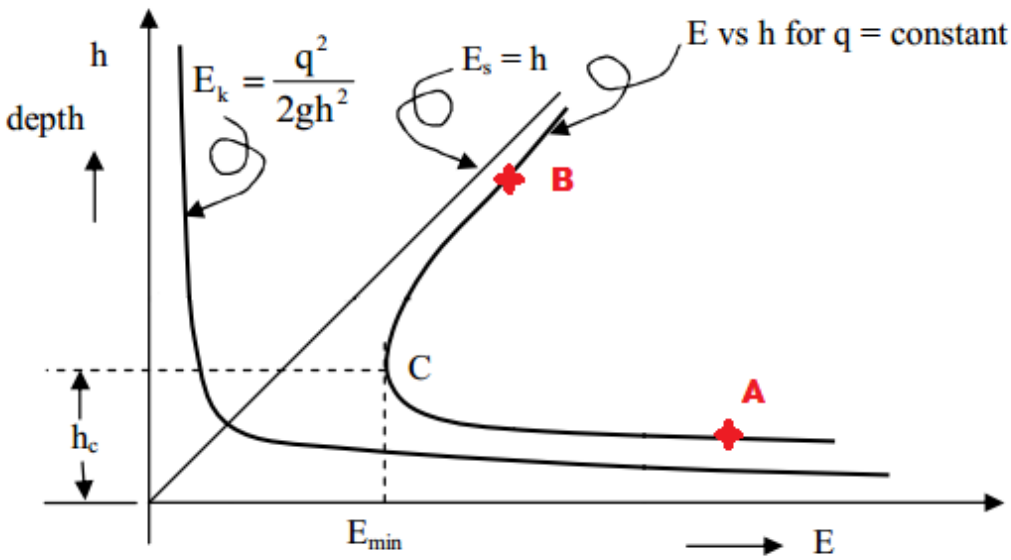

Figure 2: a plot of flow depth versus specific energy expressed in hydraulic head. Ek and Es are the kinetic energy and potential energy components of the total specific energy E. Altered after Open Channel Hydraulics for Engineers ch.3 pg. 47.

If h/h_c is lower than unity, potential energy (E_s) dominates in the flow, and the flow is subcritical. In case h/h_c is exceeds unity, kinetic energy (E_k) is the dominant form of energy, and the flow is in a supercritical flow regime.

When a flow changes from a supercritical regime, (for example point A in figure 2) to a subcritical regime (for example point B in figure 2). The energy gradient in the flow is negative at first, going from point A to point C, over the line. The energy gradient then becomes positive: going from point C to point B over the line. This positive energy gradient is physically impossible as no energy is added to the system. For this reason a change in flow from supercritical to subcritical cannot happen gradually, but has to be instantaneous (a hydraulic jump). The overall loss in specific energy whilst going from a

supercritical-flow to subcritical flow, as explained by the described theory, can be explained by the development of rollers and vortices: turbulent kinetic energy creation and dissipation.

Submerged hydraulic jumps

Hydraulic jumps are also known to occur in density flows, such as turbidity currents (Komar, 1971; Garcia & Parker, 1989; Long et al., 1990; Kostic et al., 2010). Turbidity currents are driven by their excess weight due to sediment suspended in the flow. As the Froude number is an indication between a flows inertia and gravitational forces, the component describing the forces due to gravity ought to be adjusted to a subaqueous situation as the gravity force is only applied on the excess density. The densimetric Froude number (Fr_d) describes the Froude number in a submerged setting as found in Mastbergen & Van Den Berg (2003).

$$Fr_d = \frac{U}{\sqrt{\varepsilon g H}} \qquad \text{Equation 1.4}$$

In which C is the depth-averaged sediment concentration (as fraction) and ε is the relative density difference of the sediment-water mixture:$\varepsilon = \rho_m - \rho_w / \rho_m$. Similar to the normal Froude number, a value of unity is classically expected to be the value of critical flow, this is however only valid for unstratified flows and the critical-flow Froude number differs from unity in stratified flow such as turbidity currents (Waltham, 2001).

Hydraulic jump classification

The Froude number before the hydraulic jump has implications for the intensity of the hydraulic jump created and hence, also its flow structure. If the Froude number before the jump is relatively low, little energy will be lost in the jump, and the jump will behave less vigorous than if the Froude numbers before the jump are high (table 1 provides a classification scheme of different hydraulic jumps formed at a variance of Froude numbers).

Name	Froude number	Energy dissipation	Characteristics	Illustration
Undular jump	1.0-1.7	<5%	Standing waves	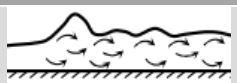
Weak jump	1.7-2.5	5-15%	Smooth rise	
Oscillating jump	2.5-4.5	15-45%	Unstable; avoid	
Steady jump	4.5-9.0	45-70%	Best design range	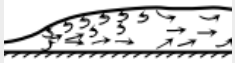
Strong jump	>9.0	70-85%	Choppy; intermittent	

Table 1: a classification scheme for hydraulic jumps as in Ven Te Chow, 1973. Illustrations from Open Channel Hydraulics for Engineers ch.3.

Bedforms in a supercritical flow-regime

Supercritical-flow currents tend to transport and erode large quantities of sediment as they typically have steeper velocity gradients in comparison to similar subcritical flows, during sediment transport several bedforms can be identified. A four-fold classification of supercritical bedforms has been proposed by Cartigny et al. (2013): stable antidunes, unstable antidunes, chutes-and-pools and cyclic step, in order of increasing peak flow intensity. Figure 3 provides a bedform stability diagram for bedforms in a supercritical flow regime (in open-channel flows).

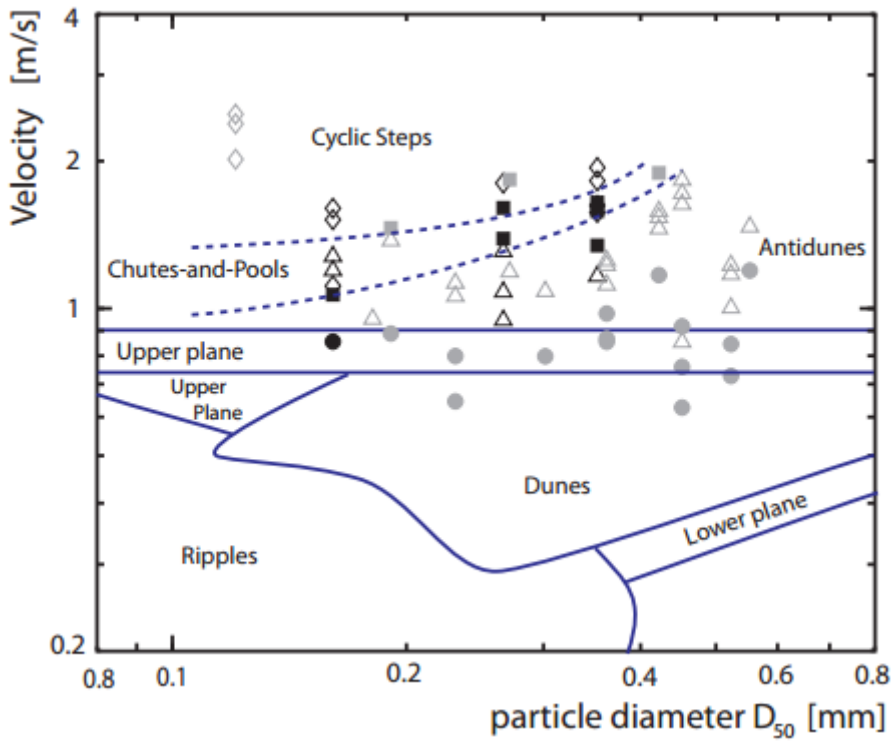

Figure 3: The bed load stability diagram from Cartigny (2012), the solid blue lines are from Van den Berg & Van Gelder (1998). The dotted lines are added by Cartigny (2012). The diamonds are observed cyclic step morphologies, squares are chutes and pools, triangles are antidunes and circles represent the upper plane bed. The data has been obtained in several studies, and different grain sizes (Gilbert, 1914; Kennedy, 1961; Guy et al., 1966; Winterwerp, 1986; Cartigny, 2012).

These supercritical bedforms are not only found in free-surface flows, but have also been observed on the sea-floor (Hughes-Clarke et al., 2012), are found in flume experiment of turbidity currents (e.g. Jorritsma, 1973; Spinewine et al., 2009) and have been modelled numerically using depth-averaged models (Fildani et al., 2006; Kostic & Parker, 2006; Kostic et al., 2010; Cartigny et al., 2011; Covault et al., 2014).

Stable antidunes

Antidunes are relatively short-wavelength, low amplitude type of bedform, associated with (near)-constant supercritical flow conditions creating in-phase surface waves and bedforms. Stable antidunes are known to move upstream or remain stationary, depending on flow intensity and grain size of the bed. (Simons et al., 1965; Hand, 1974; Alexander et al., 2001; Cartigny et al., 2013), in case of upstream migration; erosion will occur on the lee-side of the dune, and deposition on the stoss side. The antidunes are found in trains, this is observed in flume experiments and in nature as well (Simons et al., 1965; Grand, 1997; Fielding, 2006; Kostic et al., 2010; Cartigny et al., 2013).

Unstable antidunes

At flow intensities (peak Froude numbers) that are slightly higher than that of stable antidunes, unstable antidunes (sometimes referred to as breaking antidunes) can be formed. In case of unstable antidunes, hydraulic jumps periodically occur creating an upstream migrating (positive) surges that later get washed out into downstream moving (negative) surges (Kennedy, 1961; Cartigny et al., 2013). The unstable antidunes migrate upstream due to erosion on the lee-side and deposition on the stoss-side. This deposition may cause oversteepening of the stoss-side, increasing the bedform amplitude, requiring so much kinetic energy for the supercritical-flowing water to pass, that potential energy starts to dominate and a hydraulic jump (surge) develops as a result.

Chutes-and-Pools

Chutes-and-pools consist of near-planar to angle-of-repose downstream dipping surfaces over which supercritical flow scours the sediment (chutes), and troughs in which the water is in a subcritical flow regime (pools). These two stages of flow are separated by a hydraulic jump or surge. Chute-and-pool surges are not washed out downstream like the surge in unstable antidunes, but are gradually transformed in supercritical flow again. The supercritical flow on the lee-side of the bedform causes erosion, while deposition occurring in the pools, resulting in upstream migration. The upstream migration happens in a stepwise manner due to superimposed antidunes (Cartigny et al., 2013).

Cyclic steps

The cyclic steps show similarities with the chute-and-pool morphology but are found in flows of even higher peak flow intensity. A cyclic step is the highest-energy bedform found in this bedform stability diagram, see figure 3. Cyclic steps are asymmetrical bedforms, with a gentle, upstream stoss-side, and a steeper downstream lee-side, the flow regime at the stoss-side of the step is subcritical and overall depositional (Cartigny et al., 2013). The lee-side is characterised by supercritical, erosive flow over the bed. To accommodate the transition between a supercritical and subcritical flow regime, a hydraulic jump is found where slope of the lee-side decreases, and the stoss-side begins. Trains of cyclic steps migrate upstream in a stable manner (contrary to chutes-and-pools), and no other bedforms appear to be superimposed.

Methodology

To answer the posed research questions a depth-resolved numerical model is used, the numerical code used is FLOW-3D®, which is a multiphase computational fluid dynamics code based on Reynolds-Averaged Navier-Stokes (RANS) equations. The auxiliary models used here are a turbulence model (the RNG k-ε-model), and a sediment scour model. The kernel version used is the yet unvalidated FLOW-3D 11.0.0.16 beta. The FAVOR™ (Fractional Area-Volume Obstacle Representation) capabilities of FLOW-3D® version 11 allow accurate, discrete modelling of complex intra-cell fluid-sediment and free-surface-interface geometries.

The experiments of Cartigny et al. (2013) are used to validate the applicability of the code. At the same time, this provides insights in the dynamics of supercritical bedform development. The supercritical bedform development will be studied in turbidity currents as well, using the experiments of Jorritsma (1973) as a framework. To answer the first question, whether or not it is possible to simulate bedform development in a depth-resolved numerical model, the conditions described in Kennedy (1960), Kennedy (1961), Alexander et al. (2001) Cartigny et al. (2013) and the conditions as observed in the FLOW-3D® are compared. Using flow data as Froude numbers, mean water depth and flow velocity, as well as data on bed parameters as observed bedform and their

migration period, the numerical simulations will be compared to the experimental results. Once the model is validated the other aims can be approached as well.

Turbulence modelling

Turbulence is the chaotic and unstable motion that occurs in fluids when there are insufficient stabilizing viscous forces within the flow. The most elemental method to describe turbulence is by using the Reynolds number, which is proportional to the inertial forces of the flow, divided by the viscous forces, as described by equation 2.1, in which h is a characteristic flow depth, and v the kinematic viscosity of the fluid. At high Reynolds numbers, the viscous forces are unable to dampen flow instabilities this leads to the formation of eddies over a range of spatial and temporal scales.

$$Re = \frac{u*h}{v} \qquad \text{Equation 2.1}$$

Although the Reynolds number is a measure of turbulence intensity, the modelling of turbulence in an actual flow is much more complex and cannot be characterized by one scalar. There is an entire array in possibilities that can be used to describe turbulence in a flow. To describe all models and methods in great detail would far exceed the scope of this study. Hence, only a short description of the main turbulent modelling methods will be given, and the model used, the two-equation RNG model, will be elaborated upon. The methods of describing turbulence will be discussed from the most detailed one, direct numerical simulation, to the most straightforward one used in a depth averaged models. Several turbulence models can be used in FLOW-3D. FLOW-3D is a code based on Reynolds Averaged Navier-Stokes equations (RANS) so not all models are an option. The models available in FLOW-3D are: the Prandtl-mixing length model, one-equation turbulent energy model, two-equation k-ω-model, two equation k-ε model, RNG k-ε model and, the large eddy simulation model.

Direct numerical simulation

The most accurate method of simulating turbulence is direct numerical simulation (DNS). In DNS the Navier-Stokes equations are solved without any turbulence model and this implies the whole range of spatial and temporal scale must be resolved from the smallest turbulence scale: the Kolmogrov scale (η) up to the integral scale of the model. The computational costs of direct numerical simulation are very high, even at relatively low Reynolds numbers, as the number of time-steps required to be computed increases as a power law of the Reynolds number (Lee et al., 2013). For most applications turbulence closure models that do not resolve every spatial and temporal scale are valid to describe turbulence, DNS is mainly used in fundamental research on turbulence.

Large eddy simulation

Large-eddy simulation (LES) in principal is low-pass-filtering of the solutions of Navier-Stokes equations, in order to eliminate the small scale solution, which saves computational cost. This results in a filtered velocity field. Large eddies are solved explicitly and smaller eddies are accounted for using a sub-grid scale model (SGS model), and represented by an eddy-viscosity. LES can be applied to filter on spatial as well as temporal scales. Even though the only the larger scale eddies are computed explicitly, solving the Navier-Stokes equations still requires a lot of computational cost.

Two-equation k-ε model and RNG k-ε model

The two-equation k-ε model and renormalization group two-equation k-ε model (RNG-model) are based upon the turbulence viscosity hypothesis, assuming that momentum transferred by turbulent eddies can be modelled using an eddy viscosity, and solves two equations, for (1) turbulent kinetic energy (k_T) and (2) turbulent dissipation (ε_T). The turbulent kinetic energy is the energy of turbulent

velocity fluctuations, as described in equation 2.2, in which u' v' and w' are components of velocity fluctuations in the x, y and z direction, respectively. The two equations in the two-equation models allow the models to take into account history effects of the flow like convection and diffusion of turbulent energy.

$$k_T = \frac{1}{2}(\bar{u}'^2 + \bar{v}'^2 + \bar{w}'^2) \qquad \text{Equation 2.2}$$

The transport equations for turbulent kinetic energy and turbulent dissipation are the partial differential equations 2.3 and 2.4. In which P_T is the turbulent production, D_T the turbulent diffusion, these terms are calculated via yet another set of differential equations. $C_{\varepsilon T}$ is an empirically derived constant, as are the other $C_{\varepsilon x}$ variables.

$$\frac{\partial k_T}{\partial t} + \left(u\frac{\partial k_T}{\partial x} + v\,\frac{\partial k_T}{\partial y} + w\,\frac{\partial k_T}{\partial z}\right) = P_T + D_K - \varepsilon_T \qquad \text{Equation 2.3}$$

$$\frac{\partial \varepsilon_T}{\partial t} + \left(u\frac{\partial \varepsilon_T}{\partial x} + v\,\frac{\partial \varepsilon_T}{\partial y} + w\,\frac{\partial \varepsilon_T}{\partial z}\right) = \frac{C_{\varepsilon 1}\,\varepsilon_T}{k_T}P_T + D_\varepsilon - C_{\varepsilon 2}\frac{\varepsilon_T^2}{k_T} \qquad \text{Equation 2.4}$$

The empirically derived constant $C_{\varepsilon 2}$ is what makes the RNG model different from the standard two-equation k-ε model, as it is computed from the turbulent kinetic energy and turbulent production in the RNG-model.

There is a relation between the turbulent energy dissipation in the model, and the turbulent kinetic energy. Equation 2.5 describes this relation in which the maximum turbulent mixing length (TLEN) is introduced, which is a user-defined parameter. It is recommended that the TLEN is about 7% of the smallest domain dimension, the height of the stream in this case (FLOW-3D user manual: M.H. Shojaee Fard and F.A. Boyaghchi, 2007). The dynamic viscosity of the flow should however be in the order of 0-50 Pa.s, so a TLEN in the order of 0.01m is recommended (personal communication R. Rouzairol and E. Hansen). The ε_{Tmin} is a minimum value of turbulent dissipation, to prevent unphysical small values, which would lead to an overestimation of the eddy viscosity, equation 2.5 is thus purely an equation to limit unrealistic outcomes of turbulent dissipation calculated by equation 2.4

$$\varepsilon_{Tmin} = 0.085^{3/4}\,\frac{k_T^{3/2}}{TLEN} \qquad \text{Equation 2.5}$$

The turbulent kinematic viscosity (v_T) , an eddy viscosity and property of turbulent flow rather than an intrinsic material property, can be calculated from the turbulent kinetic energy and turbulent dissipation energy.

$$v_T = 0.085\,\frac{k_T^2}{\varepsilon_T} \qquad \text{Equation 2.6}$$

Using the kinematic viscosity in combination with the turbulent kinematic viscosity, the dynamic viscosity (μ) can be calculated, see equation 2.7, where v_m is the kinematic viscosity; an intrinsic material property.

$$\mu = \rho(v_m + v_t) \qquad \text{Equation 2.7}$$

The dynamic viscosity is an important parameter in the sediment dynamics, it plays a role in the drag function, Shields-Rouse equation (3.5), functions for the local Shields number (3.6) and the dimensionless particle diameter. Altogether of significant impact on the sediment transport dynamics. The sensitivity analysis done on the TLEN (and hence dynamic viscosity) also shows the

influence of TLEN on the sediment transport dynamics, this will be elaborated upon in the "model choice" segment.

One-equation turbulent energy model

The one-equation turbulent energy model is to a large degree similar to two-equation turbulence closure models. The turbulent kinetic energy is computed via equations 2.2 and 2.3. The main difference however is that the turbulent dissipation ε_T is not computed via equation 2.4 but rather is more simply related to the turbulent kinetic energy (k_T) via equation 2.8, similar to equation 2.5. The equation does not limit the partial differential equation 2.4, but replaces it to compute the turbulent dissipation.

$$\varepsilon_T = 0.085^{3/4} \frac{k_T^{3/2}}{TLEN} \qquad \text{Equation 2.8}$$

The turbulent kinematic viscosity and dynamic viscosity are calculated in the same way as in the two-equation model, via equations 2.6 and 2.7. The outcomes will however be slightly different.

Prandtl mixing length model

The simplest model which can be used in RANS-modelling and FLOW-3D is the Prandtl mixing length model. In the model the assumption is made that the fluid viscosity is increased by turbulent mixing in high-shear regions (read: near solid objects, walls, or a packed sediment bed). The model assumes that turbulence production and dissipation are in balance in every cell of the flow, meaning there can be no transport of turbulent energy over cell boundaries, leading to especially high turbulent energy values near objects.

$$P_T + G_T = \varepsilon_T \qquad \text{Equation 2.9}$$

Via equation 2.7 the turbulence dissipation is calculated in the Prandtl mixing length model as well. And the turbulent kinematic viscosity is computed in a simple equation (2.10).

$$v_T = 0.085^{1/4}\, TLEN\sqrt{kT} \qquad \text{Equation 2.10}$$

The Prandtl mixing length model is only deemed valid for stable and steady flows however (FLOW-3D user manual).

Depth averaged turbulence modelling

Although depth averaged models are not based on RANS-equations, this does not mean turbulence can be ignored. The depth averaged four-equation-model of Parker et al. (1986), is commonly used as a basis for depth-averaged modelling of turbidity currents (e.g. Kostic & Parker, 2006; Fildani, 2006 and Covault et al., 2014), depth-averaged turbulence modelling is not an option in this study, as the model used is not depth-averaged but depth-resolved. The four equations of the model describe conservation of mass and momentum, suspended sediment, and the fourth: turbulent kinetic energy. The model is discussed extensively in Kostic & Parker (2006) and this will not be done for the entire model herein. The fourth equation takes the form of equation 2.11, as described in Parker et al., (1986). Herein K is the mean turbulent kinetic energy per mass-unit, h the layer thickness, C the sediment volumetric concentration, U the flow velocity, u* is the bed shear velocity, e_w is a measure of water entrainment from the top of the flow e_w=w_e/U, in which w_e is the entrainment velocity, R is the submerged specific gravity (=1.65 for quartz), ε_0 is the mean layer-averaged rate of turbulent energy dissipation.

$$\frac{\partial Kh}{\partial t} + \frac{\partial UKh}{\partial x} = u_*^2 U + \frac{1}{2}U^3 e_w - \varepsilon_0 h - Rgv_s Ch - \frac{1}{2}RgChUe_w - \frac{1}{2}Rghv_s(E_s - r_0 C) \qquad \text{Equation 2.11}$$

The first two terms on the right-hand side of the equation represent the production of turbulent energy. The third term $\varepsilon_0 h$ represents the depth-averaged rate of turbulent energy dissipation. The Last three terms describe the loss of turbulent energy due to work against the density gradient.

Incorporating turbulence is crucial for depth-averaged modelling as well, as without the turbulent energy equations 3 and 4 of the four-equation model can create a loop self-accelerating the turbidity current. More sediment will be entrained than is settled down, resulting in a denser current, which accelerates, increases velocity and increases entrainment even more etc. etc. Energy dissipated trough turbulence is thus needed to prevent this from happening, as is the case in physical reality as well.

Model choice

Direct numerical simulation is not a method that is required in studies not focussed on fundamental turbulence research, nor is the computational power available to solve the Navier-Stokes equations without any turbulence model for the scale of this study. Large eddy simulation is available in FLOW-3D, although it provides more information on turbulence than a Reynolds averaged model. A very fine mesh is however needed and the computational cost is still too high to model the bedforms processes at the core of this study.

The two-equation models are able to model turbulence on the scale of this study within an acceptable time, meaning the model should be able to run overnight and still produce appropriate results. The two equations for turbulent energy and turbulent dissipation in the two-equation models provide reasonable approximations for many types of flows, except at inflow boundary regions (Rodi, 1980), the model also is widely used. The RNG-model is preferred over the standard k-ε-model as $C_{\varepsilon T2}$ is solved from the turbulent dissipation and – energy rather than an empirically derived constant, Sabbagh-Yazdi et al. (2007) has compared the RNG-model with the standard k-ε-model and found that the RNG-model was in better agreement with measured data.

The one-equation turbulent energy model is inferior to the two-equation models as it does not solve turbulent dissipation via a transport equation but only lets it vary with the turbulent kinetic energy. The one-equation model is not able to account for history effects of turbulence dissipation such as convection and diffusion, the two-equation models do take this into account.

The Prandtl mixing length model assumes that turbulent dissipation is in equilibrium with the turbulent production (and buoyancy) production at every grid-cell. This is only valid for steady flows, and as the formation and migration of bedforms per definition is unsteady and dynamic this model is not appropriate to use.

The depth averaged based turbulence model can obviously not be used in RANS-simulations. The depth average model assumes uniformity of flow properties over the depth of the flow.

Both the RNG two-equation model and the one-equation turbulent energy model have been tested in the simulations, and both of them allow the simulations to transport sediment in a manner such that supercritical bedforms can be formed from an initially flat bed, and are able to migrate. The model choice however has significant effects on the rate of erosion within the model. Figures 3 and 4 illustrate the difference in erosion and depositional character of one of the simulations that has been tested. The two-equation RNG-model erodes significantly more sediment at first, but after about 400 seconds an equilibrium is reached and the system becomes slightly depositional. The one-equation model on the other hand erodes less at first, but remains an overall erosional system over the entire time-span of the model. If the dynamic viscosity is examined, as in figure 5, it can be seen that in the one-equation model, dynamic viscosities are higher over the entire flow resulting in higher overall

critical shields numbers. In the two-equation model turbulence dissipates faster, leading to lower dynamic viscosities, and via the shear-stress-calculation to lower local Shields numbers and erosion (this result can be seen in figure 3).

Although both the one- and two-equation turbulence models to work, the decision has been made to use the RNG-two-equation turbulence model because of its more elaborate approximation of turbulent dissipation, while still maintaining an acceptable computational time.

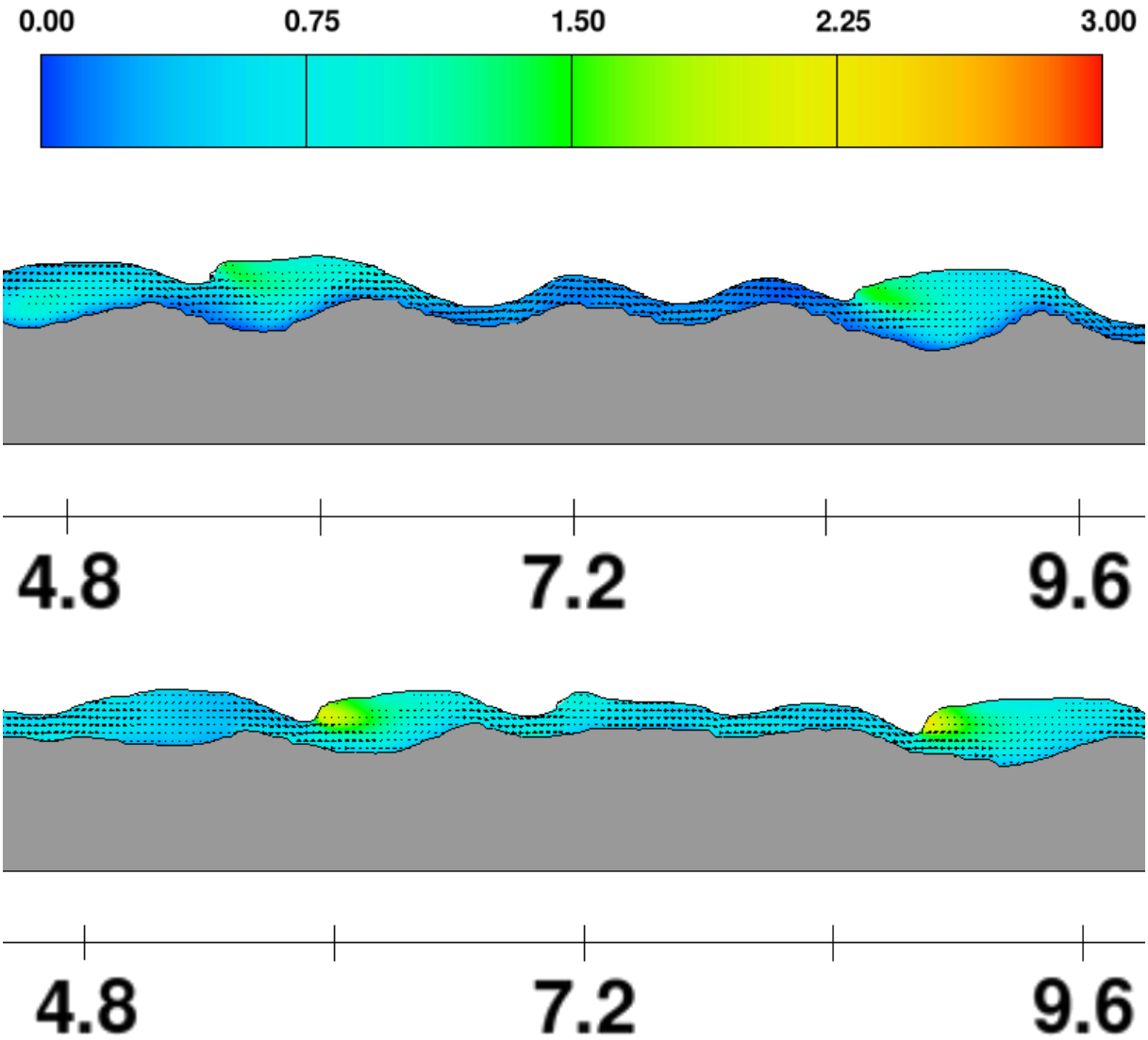

Figure 3: The dynamic viscosity (in Pa.s) of the two-equation RNG-model (on top) versus the dynamic viscosity of the one-equation turbulent energy model (bottom).

Sediment scour modelling

The sediment scour model in FLOW-3D® estimates sediment motion via erosion, transport via suspended and bed-load mechanisms and deposition by computing (1) advection, (2) settling due to gravity, (3) entrainment due to shear stresses (4) and computing bed-load transport. Sediment can exist in two states in FLOW-3D®, either as packed sediment that is unable to move, existing at its critical packing fraction, or, in a suspended low concentration.

Advection

The transported suspended sediment by advection is calculated by equation 3.1.

$$\frac{\partial c_{s,i}}{\partial t} + \nabla\left(\bar{\boldsymbol{u}} c_{s,i}\right) = 0 \qquad \text{Equation 3.1}$$

In which the velocity **u** is the mean velocity of the sediment mixture, and c the concentration of sediment.

Settling

Sediment is typically heavier than water, it will sink due to its excess density or drift, relative to the surrounding fluid. The drift rate is dependent on the balance between the buoyant forces that cause drift and drag forces which work against this drift. By combining the momentum equations for (1) the sediment species and (2) the total mixture, a new momentum equation which calculates u_{drift} can be constructed (eq. 3.2). The u_{drift} is the velocity needed to compute the transport of sediment due to drift. u_{drift} is not the relative velocity between the fluid and the sediment (which is $u_{r,i}$), but a more abstract velocity, the relative velocity between the sediment and mean velocity of the entire fluid mixture.

$$\frac{\partial u_{drift,i}}{\partial t} + \bar{u} \cdot \nabla u_{drift,i} = \left(\frac{1}{\bar{\rho}} - \frac{1}{\rho_{s,i}}\right) \nabla P - \frac{K_i}{f_{s,i}\rho_{s,i}} u_{r,i} \qquad \text{Equation 3.2}$$

In which P is the pressure, $f_{s,i}$ is the volume fraction of sediment, K_i the drag function, $\rho_{s,i}$ the density of a species of sediment, and $u_{r,I}$ the relative velocity of a species of sediment ($u_{r,i}=u_{s,i} - u_f$).

The assumption is made that sediment motion is near-steady at a computational timescale, and that pressure gradients are proportional to the acceleration of gravity. Appreciating these assumptions, equation 3.2 can be used into equation 3.3 as one if its simplified solutions for the relative velocity.

$$u_{r,i} = \frac{g}{K_i}(\rho_{s,i} - \bar{\rho}) f_{s,i} \qquad \text{Equation 3.3}$$

By solving the function for the relative velocity, and the Stokes drag function, the $u_{drift,I}$ can be computed in equation 3.4.

$$u_{drift,i} = \left(1 - f_{s,i}\right) u_{r,i} - \sum_{j=1}^{N(-i)} f_{s,i} u_{r,i} \qquad \text{Equation 3.4}$$

Entrainment

Sediment is entrained in the water if the local shear stress exceeds the critical shear stress at a given location. Entrainment cannot be calculated for each individual grain so empirical formulas are used. The critical shear stress at a given location is a function of the densities of the fluid and the sediment, the grain size of the sediment and the (dynamic) viscosity of the fluid, this is done via the Shields-Rouse-equation of (Gou, 2002), equation 3.5. Additionally, the model also deals with the effect of armouring, in which larger grains “protect” smaller ones, and the model corrects for the bed slope. The equation describing the model for the critical shear stress create an algorithm to solve the critical Shields stress at a given point in time and space.

$$\theta_{cr,i} = \frac{0.1}{R_i^{*2/3}} + 0.054\left[1 - \exp\left(\frac{-R_i^{*0.52}}{10}\right)\right]$$ Equation 3.5

In which R* is a dimensionless parameter defined as: $R^* = d_{s,i}\left(\frac{\sqrt{0.1(\rho_{s,i}-\rho_f)\rho_f\|g\|d_{s,i}}}{\mu_f}\right)$

The local Shield number is calculated based on the local shear stress, and given by equation 3.6.

$$\theta_i = \frac{\tau}{g d_{s,i}(\rho_{s,i}-\rho_f)}$$ Equation 3.6

In which the local shear stress is divided by the product of the gravitational acceleration, grain size and density difference of the grains. High shear stress, low relative density of the grains, or small grain sizes will thus lead to higher local Shields numbers and hence, more sediment entrainment.

The local shear-stress is represented by a stress tensor in the Navier-Stokes equations, in short though: it can be said that the local shear stress is a product of the viscous forces and the shear velocity (equation 3.7), where μ is the dynamic viscosity and $\frac{du}{dz}$ the shear velocity, this is not exactly how the shear stress is calculated in FLOW-3D but merely an illustration.

$$\tau = \mu\frac{du}{dz}$$ Equation 3.7

The entrainment lift velocity (u_{lift}), which also is a volumetric flux, of the sediments is then calculated in equation 3.8, and is a function of both the local shields number (Θ_i), critical shields number ($\Theta_{cr,i}$), gravity (g), the differences in density ($\rho_{s,i}$-ρ_f), and dimensionless grain size (d*). There is also is an entrainment coefficient involved in equation 3.7 (α_i), it has a default value of 0.018 (corresponding with Mastbergen and Van Den Berg, 2003). Higher values for the entrainment coefficient lead to more sediment entrainment. This entrainment coefficient can be altered in the physics module of the FLOW-3D sediment scour model.

$$u_{lift} = \alpha_i n_s d_*^{0.3}\left(\theta_i - \theta_{cr,i}\right)^{1.5}\sqrt{\frac{\|g\|d_{s,i}(\rho_{s,i}-\rho_f)}{\rho_f}}$$ Equation 3.8

Bed-load transport

The model for bed-load transport in FLOW-3D is based on the Meyer, Peter and Muller equation. It predicts the volume of sediment that flows over the packed bed interface. First of all, a dimensionless bed-load transport rate is calculated, which is a function of the critical and local Shields number, critical Shields number, and a bed-load coefficient, this again is a parameter which can be changed in the FLOW-3D scour model, the default value is set to 8: a higher value would lead to more transport. Equation 3.9 computes the volumetric bed-load transport rate (volume per unit width over time), the first term of which is the dimensionless bed-load-transport-equation, β_i is the bed-load coefficient.

$$q_{b,i} = \beta_i(\theta_i - \theta_{cr,i})^{1.5} * \left[g\left(\frac{\rho_{s,i}-\rho_f}{\rho_f}\right)d_{s,i}^3\right]^{\frac{1}{2}}$$ Equation 3.9

The thickness of the bed-load layer is calculated via the grain size of the sediment, critical and local Shields number in equation 3.10, and the fraction of sediment in bed-load transport in the cell in equation 3.11.

$$\frac{\delta_i}{d_{50}} = 0.3 d_*^{0.7} \left(\sqrt{\frac{\theta_i}{\theta''_{cr,i}} - 1} \right) \qquad \text{Equation 3.10}$$

$$f_{b,i} = 0.18 \frac{f_{packed}}{d_*} \left(\frac{\theta_i}{\theta''_{cr,i}} - 1 \right) \qquad \text{Equation 3.11}$$

This allows equation 3.12 to compute the velocity of the bed-load ($u_{bedload}$), in which the volumetric bed-load transport rate is divided by the height of the layer δ_i, and the volume fraction of sediment $f_{b,i}$.

$$u_{bedload} = \frac{q_{b,i}}{\delta_i f_{b,i}} \qquad \text{Equation 3.12}$$

The volume fraction of sediment in the bed-load-layer is empirically obtained, it is a function of the packed sediment fraction, grain size, and local and critical Shields numbers. A $\mathbf{u_{bedload}}$ vector is created. The resulting mass-flux of the model is described in equation 3.13. In which δ_i is the thickness of the bed-load layer, $f_{s,i}$ the volume fraction of sediment and $\rho_{s,i}$ the density of the sediment.

$$Q_{b,i} = u_{bedload} \delta_i f_{b,i} \rho_{s,i} \qquad \text{Equation 3.13}$$

Combining the four computed sediment scour components allows for an estimation of the sediment transport via the scour model in FLOW-3D.

Model setup: free-surface flow

The first simulations performed are done using a free-surface flow (i.e. subaerial open-channel flow), the model is constructed to have dimensions similar to that of the Eurotank flume laboratory in Utrecht. The resulting data of the model can then be compared to the physical experiments as described in Cartigny et al. (2013). Details on the exact conditions used can be found in Cartigny et al. (2013) and are not reiterated here.

Mesh

The meshed area is 12m x 0.15m x 1m (x,y,z). The number of cells in the x-direction is 360, implying a cell size of 3.3cm. The number of cells in the y-direction is 3, corresponding to a 5cm cell size. In the z-direction 35 cells are present, the minimum size of which is 1.8cm (at the bed-fluid interface), and the maximum size is 8.5cm. Aspect ratios stay limited to 2.5 at a maximum. The physical experiment had a y-scale of 0.48m, but in order to limit computational time, the number of cells in the y-direction is limited to 3, making it a de facto 2D model.

Geometry

The inlet for the water is located in the top left of the model and is of a weir-type. This allows the fluid-sediment mixture to flow in and over the bed, and create its own equilibrium slope as there is no realistic limit to the height of the bed on the inlet boundary of the model. On the right-hand-side an outflow is created with a small obstacle placed below the bed, this is to prevent excessive erosion caused by the flow. In the experiments of Cartigny et al. (2013), a standing body of standing water is located at the outlet, this slows down the flow and allows for deposition after erosion. The body of ambient water was too difficult to mimic correctly so a wedge-shaped object is placed below the bed

to slow the water instead and prevent erosion of the entire bed. Figure 4 displays the setup of the model in an X-Z cross-section.

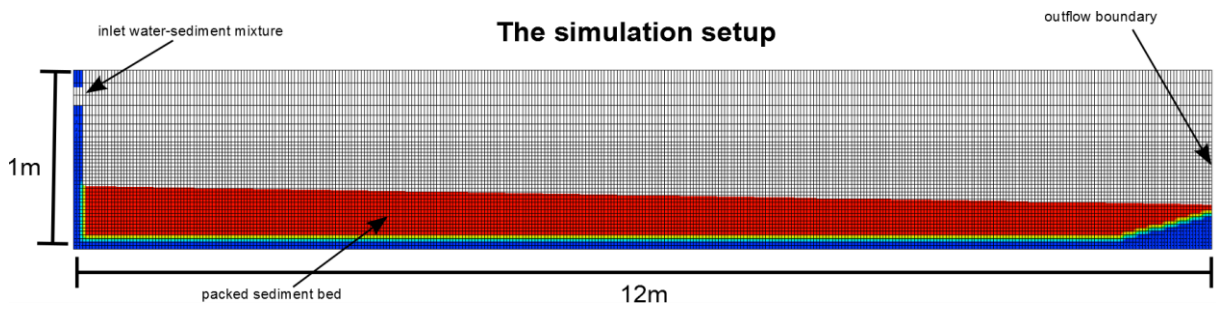

Figure 4: The model geometry with inflow on the bottom left, and outflow on the right. The red component in the packed sediment bed, the blue component is a solid non-erodible object. Scale is in meters and the flow is from left to right.

Boundary conditions

The Xmin inflow boundary condition is a specified flow velocity and height, generally corresponding with discharges as described in the physical experiments of Cartigny et al. (2013) or Alexander et al. (2001). Unfortunately neither of the authors provide inflow sediment concentrations, as a recirculating tank is used. The Xmax has an outflow boundary condition. Ymin and Ymax are symmetry boundaries, implying a free-slip boundary. The Zmin boundary is a wall, an object with sediment-sized surface roughness is also placed below the sediment bed in case the flow erodes to the flume floor. The Zmax boundary is a specified pressure of 0 Pascal differential pressure and a fluid fraction of 0 (the air above the free-surface).

Physics

The gravity is -9.81 m/s² in the z-direction. Within the scour model, the grain size is differed between 160 and 450 µm. The bed-load coefficient (BLC) is set to 4 (Wong & Parker, 2006), the entrainment coefficient to a default 0.018, drag coefficient to 0.5, and angle of repose of 30 degrees. The turbulence model used is the RNG k-ε-model with a TLEN of 0.005m, which yielded realistic dynamic viscosities between 0-1Pa.s.

Output and numerics

The simulations will run for 1800 seconds each, of which the first 200 seconds are usually required to reach a macroscopic slope and flow equilibrium. Data is saved every two seconds leading to 900 time-steps to be analysed per simulated run.

Model setup: turbidity current

The turbidity current model has a larger modelled volume than the free-surface flow, the main reason for this is that mean equilibrium slopes are higher and the model thus needs to be larger in the z-direction. Not as many simulations have been run in the turbidity current cases as in the free-surface model. The validity of the FLOW-3D® model in subaqueous cases is not tested against physical experiments as thoroughly as in the free-surface flows. The data of Jorritsma (1973) is used as a framework however.

Mesh

The mesh of the turbidity current simulation is larger than in the free-surface flows. The mesh is 24x0.15x2m (x,y,z). With 920 cells in the x-direction, 3 in the y-direction and 67 in the z-direction.

Averages cell size is are 2.6cm x 5cm x 2cm (x,y,z) in the interesting areas where bed-interaction occurs.

Geometry

The inlet is different than in the free-surface case. A jet-type inlet is used to prevent excessive erosion on the bed directly at the inlet. A 2 degrees inclined bed is used. The model is filled with ambient water to the top. Figure 5 visualizes the geometry.

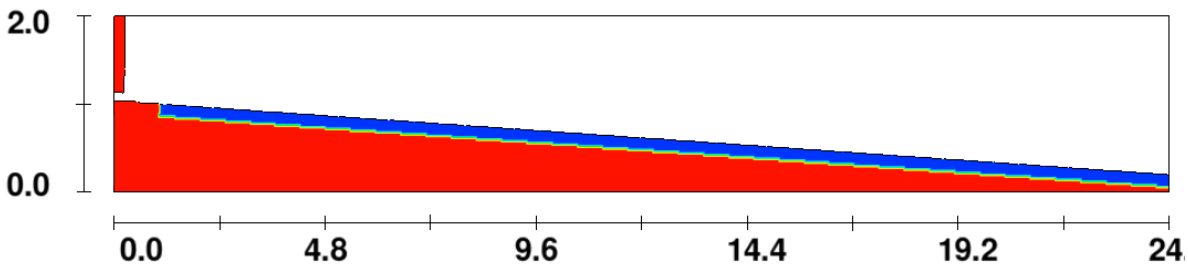

Figure 5: A visualization of the setup of the subaqueous simulations. The blue component is a 140um packed sediment bed, the red components are solid non-erodible objects.

Boundary conditions

The inflow boundary condition on the Xmin boundary is specified as a fixed 1.1 m/s velocity of a 1200 kg/m³ water-sediment mixture through a 10-cm high inlet, corresponding with discharges of Jorritsma (1973)'s run 10. The Xmax is an outflow boundary condition. Ymin, Ymax and Zmin are walls and Zmax is a specified 0Pa differential pressure with fluid fraction 1 at the top.

Physics

The scour model uses 140µm sediment, all other physical parameters are similar to those used in the free-surface model

Output and numerics

The simulations will run for 500 seconds each, and data is saved every second, the simulation is only 500 seconds because the model is larger, and this way an acceptable computing time is still maintained.

Data analysis

The results of the modelled simulations were analysed in a 2D X-Z plane as well as using a 1D probe time-series at fixed locations every 1m the main locations used however are the x=2m, x=8m (the same distance Cartigny et al. 2013 used for analysis of 1-D flow data) and, near the end of the flume (x=10m).

The flow data from the stationary 1D-probes is analysed using Matlab®. Parameters investigated are the 50th and 90th percentile of the Froude numbers, as illustrated in figure 6, the Matlab script used can be found in appendix 2. The local Froude number is a given output value by FLOW-3D and corresponds with equation 1.1. The depth averaged velocity 50th and 90th percentile have been

obtained in a similar manner.

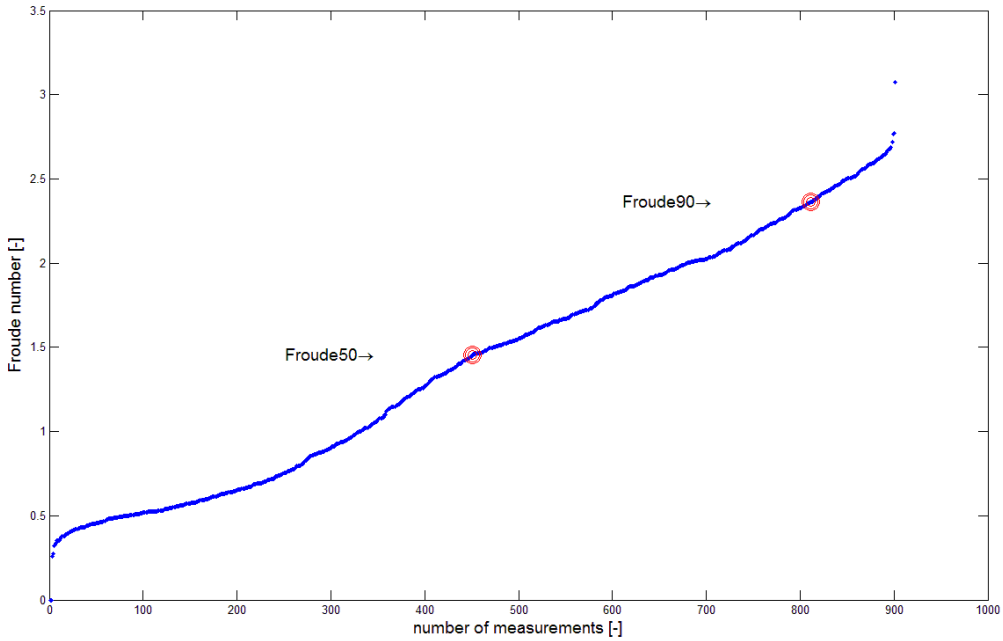

Figure 6: a graphic illustration of how the Froude 50 and 90 have been identified in the Matlab scripts. A cumulative distribution of the Froude numbers observed over the run on a fixed location. The curve is used to extract parameters such as Froude median and 90th percentile.

The period of bedform migration has been obtained via a discrete Fourier analysis on the time-series (Cartigny et al., 2013). Details on the calculations can be found in appendix 2.

Normalized mean plots of several flow- and bed properties have been made, at which averaging over multiple cyclic steps is done. The time-normalization is needed to construct plots of flow and bed properties over multiple cyclic steps which do not have the exact same period of migration. In this way average flow properties and bed properties can be analysed rather than individual ones, individual bedforms can show a significant amount of variance to one another. The fixed location probe data has been used for the time-normalization, the time between two bedform-peaks has been normalized to 1000 normalized time units, as the rate of bedform migration varies slightly. In order to allow this time-normalization, interpolation between several points has been done. Appendix 3 provides the basic calculations of the time-normalization procedure in Matlab.

The turbidity current cases require additional calculations of the Froude number, as FLOW-3D® does not provide densimetric Froude numbers. The densimetric Froude number has been calculated using a depth-averaging method and the depth-integrated method as described in Garcia & Parker (1993), the Matlab scripts elaborating on the methods can be found in appendix 4.

Results: free-surface flow

Model verification

It is important to use a valid model in numerical simulation, otherwise the results have no physical basis, and are thus useless. The first aim was thus to test the validity of the used depth-resolved numerical model, this is done for free-surface flow using physical experimental data from Kennedy (1960), Alexander et al. (2001) and Cartigny et al. (2013). During simulation 1, a specific discharge of 0.093m²/s with a sediment concentration of 150kg/m³ is set as the inflow condition. The system is allowed to create its own equilibrium slope (which reaches ~1.6 degrees on average). The discharge conditions correspond closely (within 5%) with several of Cartigny et al. (2013)'s runs: 11, 12, 15 and 16. All of Cartigny et al., (2013)'s runs yielded different bedforms: antidunes, chutes-and-pools, cyclic steps and cyclic steps. The results of all simulations at all locations analysed can be found in appendix 1. Simulation 1 resulted in an equilibrium slope after approximately 300 seconds (see figure 7).

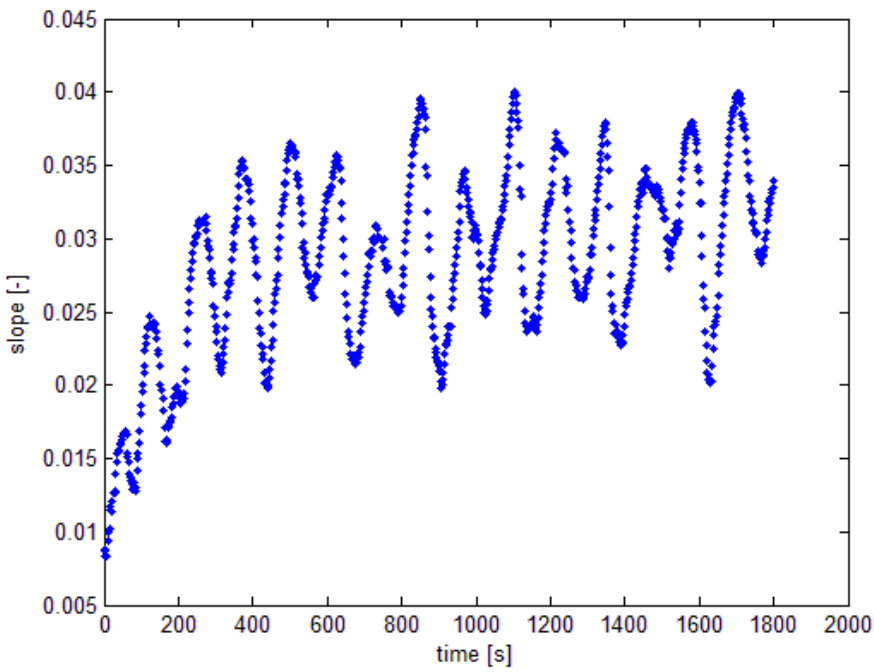

Figure 7: temporal evolution of the mean slope of the entire simulation

Proximal

The results are divided in proximal, mid and distal probe locations because the results appear to differ somewhat over the distance of the model. It is interesting to investigate what causes these differences in flow-properties and bed-properties at different locations in the model. The proximal measurements are closest to the inlet (x=2m), the mid-measurements are at x=8m and the distal measurements at x=10m.

The bedforms developed in the proximal, relatively high-slope (2 degrees) part of the model setup appear to be cyclic steps. Cyclic steps have been identified by their characteristic of having a constant hydraulic jump present. A saw-tooth Froude-number pattern with very regular bedform migration can be observed in the time-series (figure 9). The Fr_{50} and Fr_{90} are far apart as is seen in the experiments that yielded cyclic step morphologies (1.31 and 2.04), in the numerical simulation this is slightly more (1.05 and 2.38). Appendix 1 shows all parameters of known of experiments of

Alexander et al. (2001) and Cartigny et al. (2013), a comparison also show the proximal bedforms in simulation 1 closest resemble cyclic steps.

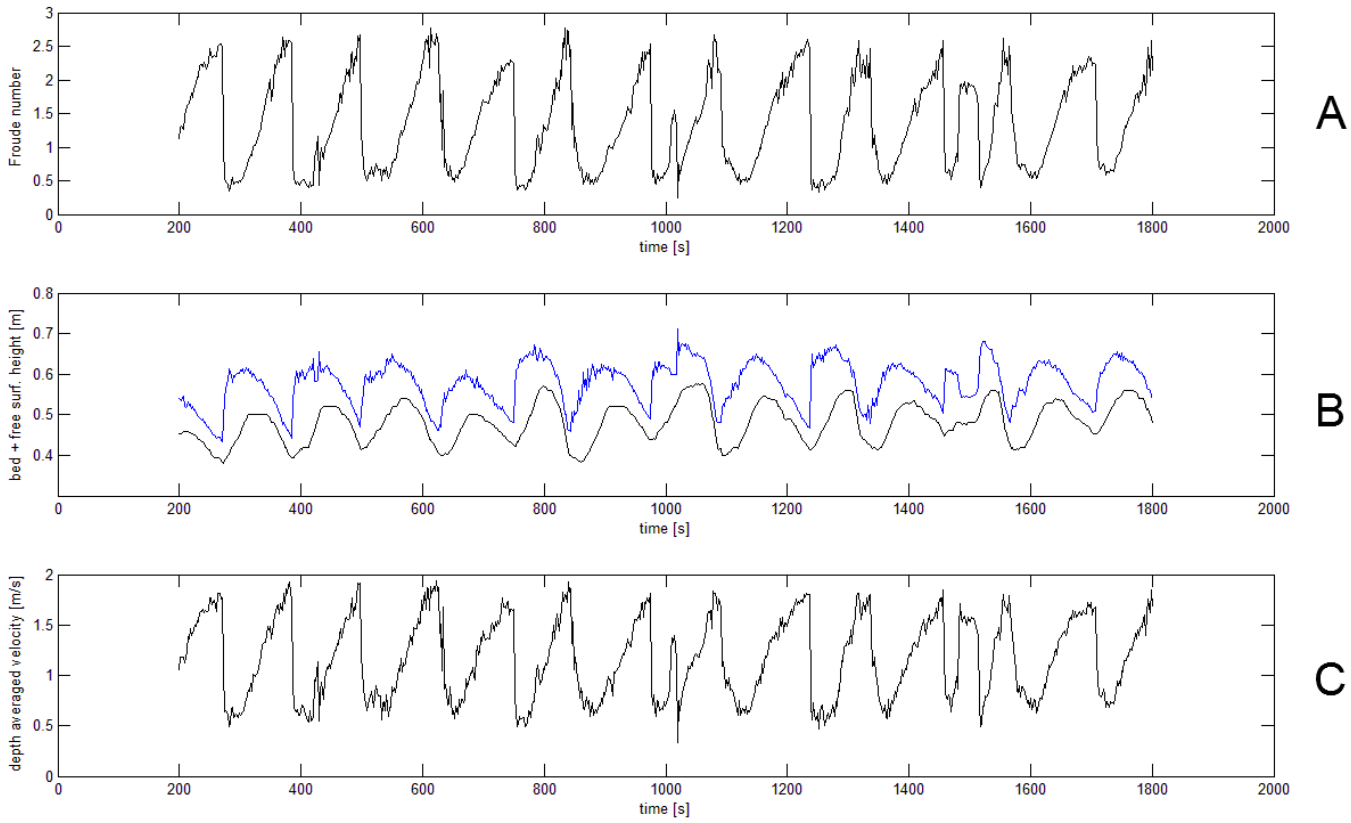

Figure 9: time-series data on Froude number (subfigure A), bed and free-surface elevation in m (subfigure B) and depth-averaged velocity in m/s (subfigure C), sample location at x=2m in simulation 1.

Distal

In the distal parts of the experiment the time-averaged mean local slope of the bed becomes slightly lower ~1.5 degrees. The time-series of Froude-number, bed-height, free-surface elevation and depth-averaged velocity are much more irregular and do not display a pattern as clear as in the proximal area. The flow first creates wavy bedforms in a continuously supercritical regime. The bedforms however appear to increase in amplitude and become oversteepened, after tens of seconds and the smooth free-surface waves break as a consequence. The bedforms go through phases of hydraulic jump development and upstream migrating surges that get washed out downstream after a several seconds before a new hydraulic jump develops, the cycle has a period of about 120 seconds. Wavelengths of the bedforms in the distal area are more variable, and on average slightly shorter than more proximal, although they are in same order of magnitude (1.5-2.5m).

The properties and dynamic behaviour as observed and described in the distal parts of the simulation appears to correspond with antidune dynamics as described by Kennedy (1961). To confirm whether the bedforms in the distal area of the model are actual (unstable) antidunes, their geometries and flow-parameters are compared with the existing literature: Kennedy (1960), Kennedy (1961), Alexander et al. (2001) and Cartigny et al. (2013). The properties of the flow, geometries of the bedforms and rates of migration are compared to investigate which bedforms are observed.

Comparison geometries of Kennedy (1960 & 1961) and Alexander et al. (2001)

Kennedy (1961) provides an empirical relation between flow parameters and antidune wavelength

$$Fr^2 = \frac{cosh^2(kd)}{kd(\sinh(2kd)+kd)} \qquad \text{Equation 4.1}$$

In which d is the flow depth and k the wave number, a measure of wavelength in which k=2π/L (where L is the wavelength), Fr is the Froude number. Kennedy (1960) provides an empirical relationship between antidunes wavelength and depth-averaged velocity (4.2).

$$v = \sqrt{gL/2\pi} \qquad \text{Equation 4.2}$$

Alexander et al. (2001) has produced upstream migrating antidunes with wavelengths of 0.76-1.14m. Flow conditions are: a mean flow depth of 0.069m and Froude number of 1.7, L=1m will be used as an average wavelength. Entering the wavelengths in equation 4.1 yields a Froude number of 1.11 minimum and 1.60 maximum (see table 1). This is too low to correspond with the actual values as described Alexander et al. (2001), 65-95% of measured values (5-35% too low), but in the right order of magnitude. A similar result is seen for the velocities as expected via equation 4.2, 75-95% of measured values (5-25% too low). If the wavelengths were slightly higher (L=1.3m) or the flow depth slightly less ~0.06m, values would correspond closer.

In the proximal simulations, the Froude numbers predicted by equation 4.1 are much higher than the actual measured data 1, 25% to 110%. The flow velocities display similar values between measured velocities and expected velocities from equation 4.2 if there were to be an antidune morphology.

To verify an antidune interpretation for the bedforms observed in the middle and distal part of the simulation, the theoretical flow properties are compared to the observed flow properties.

For the middle part of the simulation, values of Froude numbers from the equation get closer to the actually measured mean Froude number, almost no difference in the absolute lowest case, up to 95% too high at maximum wavelengths. The predicted velocities also show no difference in the low case but a difference up to 65% in case maximum wavelengths are used.

Distally, the overestimation of predicted values by equation 4.1 and 4.2 is still present, but not as high as before Froude number values predicted by the equation range from 7% too low, to about 55% too high, but a mean difference of 17%. Estimated velocities by equation 4.2 are closer in range too but still 11 to 45% too high.

The bedforms found in the distal area are likely not stable antidunes, the flow-parameters (especially the lack of a constant hydraulic jump) also suggest they are not stable cyclic steps. They are more likely an intermediate form breaking (unstable) antidunes or chutes-and-pools rather than cyclic steps or antidunes by interpretation of the relationships proposed by Kennedy (1960, 1961).

	wavelength (Min-mean-Max)	mean flow depth	Actual depth-averaged flow velocity (m/s)	mean Froude number (measured)	Froude number (eq4.1) Min—mean-max	Velocity (eq4.2) Min-mean-max
Alexander et al. (2001) run 1 and 2	0.76-1-1.14	0.069	1.40	1.7	1.11-1.41-1.6	1.08-1.24-1.33
Simulation 1 proximal	1.5-2.2-2.6	0.1	1.07	1.15	1.44-1.97-2.42	1.53-1.85-2.01
Simulation 1 Mid	1.4-2.1-2.8	0.09	1.26	1.48	1.49-2.20-2.90	1.47-1.81-2.09
Simulation 1 distal	1.3-1.7-2.3	0.09	1.30	1.50	1.40-1.78-2.38	1.42-1.62-1.90

Comparison flow data of Alexander et al. (2001) and Cartigny et al (2013)

Not only the empirical theoretical relations of bedforms and flow properties of Kennedy (1960,1961) can be used to gain further insights into which bedforms have been simulated, the more recent flume experiments of Alexander et al. (2001) and Cartigny et al. (2013) will be used as well, as a lot of data is available.

Taking into account the flow parameters as Froude numbers and flow velocities (appendix 1) it is clear that the Fr_{50} and Fr_{90} distally are closer together than in proximal cyclic step cases, this can be represented by an Fr_{90}/Fr_{50}-ratio. For antidunes the Froude numbers should be close together: a ratio between 1.07 and 1.33 has been observed in Cartigny et al. (2013), the ratio observed in the distal part of the simulation however is in the order of 1.4. An explanation would be that the bedforms in the distal area are neither cyclic steps, nor stable antidunes (which do not display hydraulic jumps at all), but unstable, breaking antidunes or chutes-and-pools. Bedforms described as unstable antidunes in literature Cartigny et al. (2013), have an Fr_{50}/Fr_{90}-ratio of about 1.2. The bedforms appear to be breaking (unstable) antidunes to the eye, but the Froude number suggest they are in between cyclic steps and unstable antidunes.

Chute-and-pool morphologies are thought to be a type of bedform where unstable antidunes are superposed on larger wavelength cyclic steps. The Froude number distribution resembles the simulations in the distal case much closer; a ratio between 1.3 and 1.6. Chutes-and-pools also display an alteration between hydraulic jumps that behave as upstream migrating surges, alternating with Froude-supercritical flow lacking a hydraulic jump (Cartigny et al., 2013). Taking into account the differences in Fr_{50} and Fr_{90} the observed bedforms more distally closest resemble chutes-and-pools.

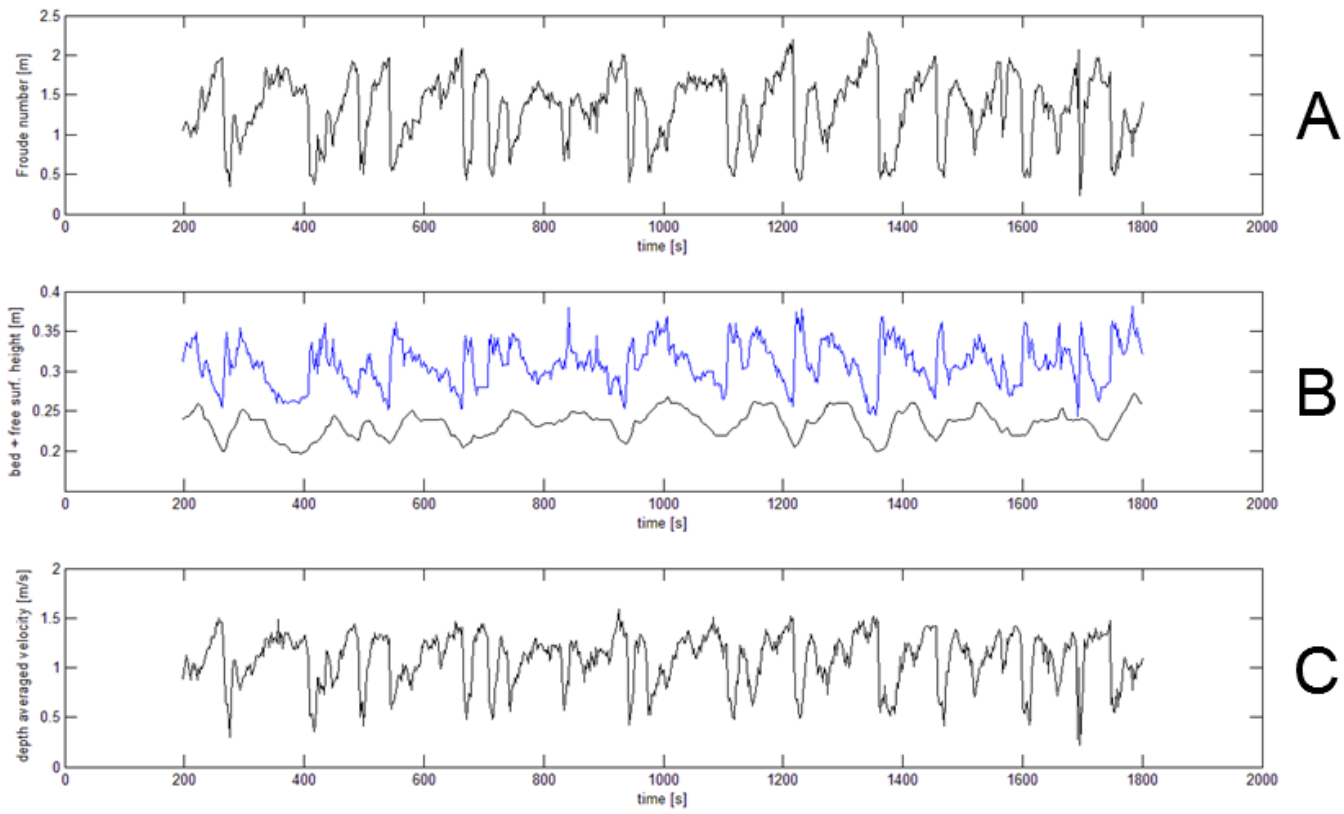

Figure 10: Froude number (A), bed elevation (B in black) free-surface elevation (B in blue) and depth-averaged velocity (C) at a stationary distal point in the model setup (x=11m).

Frequency analysis

The period of bedform migration is different for each type of bedform (Cartigny et al., 2013). To further support the hypothesis that the bedforms located proximally can be interpreted as cyclic steps, and more distally can be interpreted as being chutes-and-pools, a Fourier transform is done on the bed and free-surface data in order obtain periods of bedform migration, even if different waveforms are superimposed on one another.

The proximal bedforms display an average bedform migration period of 118 seconds; within realistic values for cyclic steps, as observed in flume experiments (Cartigny et al., 2013). In the mid case, a bed-migration period of about 130 seconds is dominant. The free-surface however also displays a secondary period, an irregular one of 30-60 seconds (see figure 11). In the distal area the bedform migration period of 118 seconds is the only frequency observed again. Overall it can thus be said that the rate of bedform migration does not change from distal to proximal in the simulation. The rates of bedform migration at all locations correspond closest to those of cyclic steps. If the bedforms more distally were to be chutes-and-pools or unstable antidunes, as suggested by comparing the data with that of Kennedy (1960), Kennedy (1961), Alexander et al. (2001) and Cartigny et al. (2013), their period of migration is expected to be 200-250 seconds (Cartigny et al., 2013), about double that of what is observed in the simulation, whilst similar conditions as specific discharge and grain size have been used.

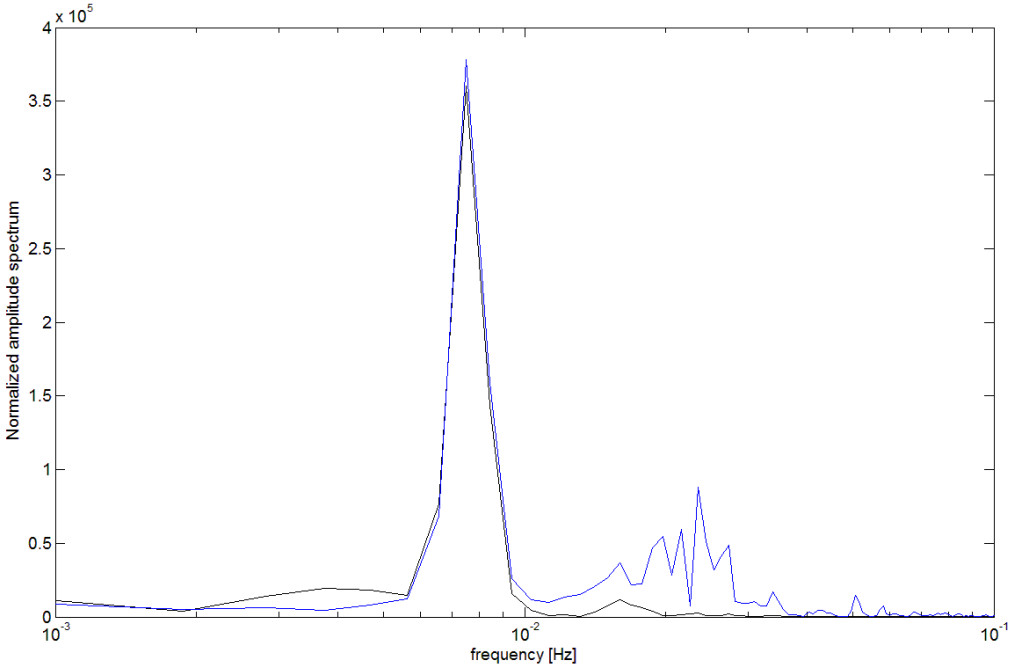

*Figure 11: a frequency analysis of the frequency distribution of bedforms (black line) and free-surface elevation (blue line) in simulation 1, the mid-case (x=8m). The high peak at ~3*10^{-2} Hz frequency is the 130 sec. period, the other, more scattered peak around 8*10^{-1} Hz frequency is the 30-60 period of the free-surface.*

Unidentified supercritical bedforms

In summary, the proximally observed bedforms are here interpreted as cyclic steps, due to their good fit with both flow-properties and bed-parameters. The more distal bedforms cannot unambiguously be interpreted as a type of bedform, their morphology closest resembles that of cyclic steps, whilst flow-properties suggest the bedforms are either chutes-and-pools or unstable antidunes, rates of bedform migration however suggest it is unlikely the bedforms are chutes-and-pools or unstable antidunes. The bedforms observed more distally will herein thus be referred to as unidentified supercritical bedforms (USBs).

Equilibrium conditions for bedform formation

The second aim of this study is investigating at which equilibrium conditions certain bedforms are formed and maintained in a supercritical-flow regime. In order to prevent confusion on the use of the term equilibrium condition, the following assumption has been made: the equilibrium conditions at which different bedforms are stable, stable does not mean stationary as the bedforms migrate, a maintenance of the bedform type (and morphology) is meant; equilibrium on a macroscopic scale.

Bedforms

Three types of bedforms were observed in the simulations: cyclic steps (defined by have a constant and stable hydraulic jump), undefined supercritical bedforms that do not clearly match with any of the categories of the from a supercritical stability diagram, but resemble chutes-and-pools closest, and a (upper stage) plane bed. The formation of the different bedforms are here controlled by three independent variables: grain size, specific discharge and sediment inlet concentration.

There are two dependent variables that seem to give a good indication of whether or not the development of cyclic steps is likely. First: the ratio between the Fr_{90} and Fr_{50}, both in the simulations as in the experimental data, this is a good indicator of the development of cyclic steps, if the ratio

exceeds values of about 1.6, then cyclic steps can be expected. This can be observed in figure 15. The Fr_{90}/Fr_{50} ratio gives a good indication because of the hydraulic jumps associated with cyclic steps, the supercritical (thin) flow over the lee-side of a step creates relatively high Froude numbers while the subcritical stoss-side of the jump results in relatively low Froude numbers. If the Fr_{90}/Fr_{50} is high; stable hydraulic jumps are present, an excellent indication of cyclic steps as bedforms. Secondly, the slope appears to correlate with the type bedforms; mean slopes that exceed about 2 degrees in the developed cyclic steps, whereas lower slopes only develop the undefined supercritical bedforms. There also seems to be a correlation between high slopes and high Fr_{90}/Fr_{50}-ratios, figure 12 visualizes the correlations between the different bedforms, the slope and the Fr_{90}/Fr_{50}-ratio.

The mobility parameter (Θ_{90}) of Van den Berg & Van Gelder (1993) may show some correlation with observed bedform for the physical experiments of Cartigny et al. (2013) (see figure 13), but fails to provide a clear pattern in the simulations. Θ_{90}-values in the simulations are consequently much lower than those in the experiments, they never exceed 2.3 whereas values up to 9 may be reached in similar experimental settings.

$$\theta_{90} = \frac{\rho u_{90}^2}{(\rho_s - \rho)(C'_{90})^2 D_{50}} \qquad \text{Equation 5.1}$$

Where D_{50} is the mean grain size, u_{90} the 90th percentile flow velocity, ρ and ρ_s the fluid and grain density and C_{90}' (Chézy coefficient as h represents flow depth) is defined as:

$$C'_{90} = 18 \log\left(\frac{4h_{10}}{D_{90}}\right) \qquad \text{Equation 5.2}$$

Figure 13 is a display of the Fr_{90}/Fr_{50}-ratio versus the mobility parameter. In the experiments of Cartigny et al. (2013) (in blue) both parameters show some correlation with bedforms, high Fr_{90}/Fr_{50}-ratios and high mobility parameters both result in bedforms higher up in the supercritical bedform stability diagram. The simulations (in red) show this trend in the Fr_{90}/Fr_{50}-ratio, but not in the mobility parameter (equations in Van den Berg & Van Gelder, 1993, 5.1 and 5.2 herein), similar bedforms are created at a narrow range of mobility parameters between 1 and 2.5, in contrast to the mobility parameters in the physical experiments that reach values up to 9.

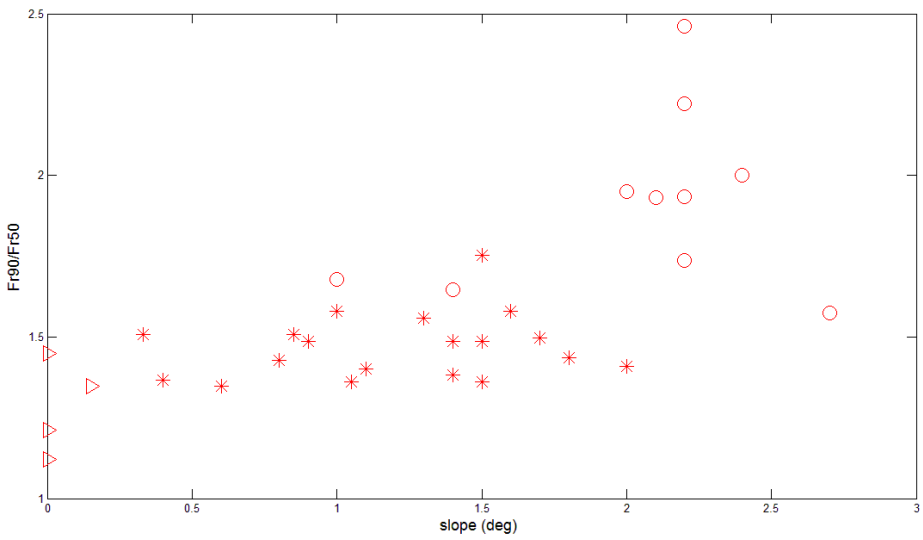

Figure 12: Fr_{90}/Fr_{50}-ratio plotted against slope. The marker symbols indicate different types of bedforms. The circles are cyclic steps, the stars are the ambiguous undefined supercritical bedforms and the triangles indicate a flat (upper stage plane) bed.

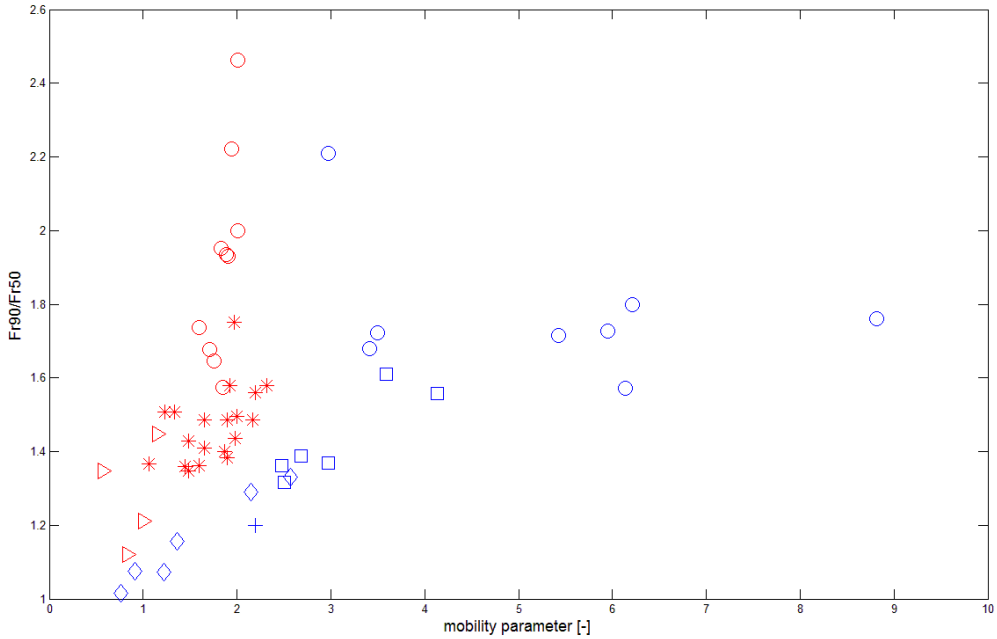

Figure 13: All bedforms as markers plotted in an Fr_{90}/Fr_{50} versus mobility parameter (Van den Berg & Van Gelder, 1993) diagram. The red markers are from the simulations, blue markers are from Cartigny (2013)'s experiments. Circles are cyclic steps, squares chutes and pools, stars unidentified supercritical bedforms, diamonds are antidunes and the plus-sign represents a breaking antidune morphology.

Discharge effects

The first independent variable that is investigated is the specific discharge (discharge per unit width) which may have significant effects on the developed bedforms and their stability. The effect of specific discharge is tested over a series of simulations. Simulations 2, 4 and 6 have different specific discharges from simulation 1, other than that all parameters are the same, details can be found in appendix 1

The effect of an increased (specific) discharge appears to be that of an increase in mean equilibrium slope in general. Up to discharges of about 0.1m²/s slopes gradually increase with discharge. Simulation 4 which has a discharge of 0.12m²/s breaks the trend and has a slightly lower slope on average than the previous measurement (figure 14).

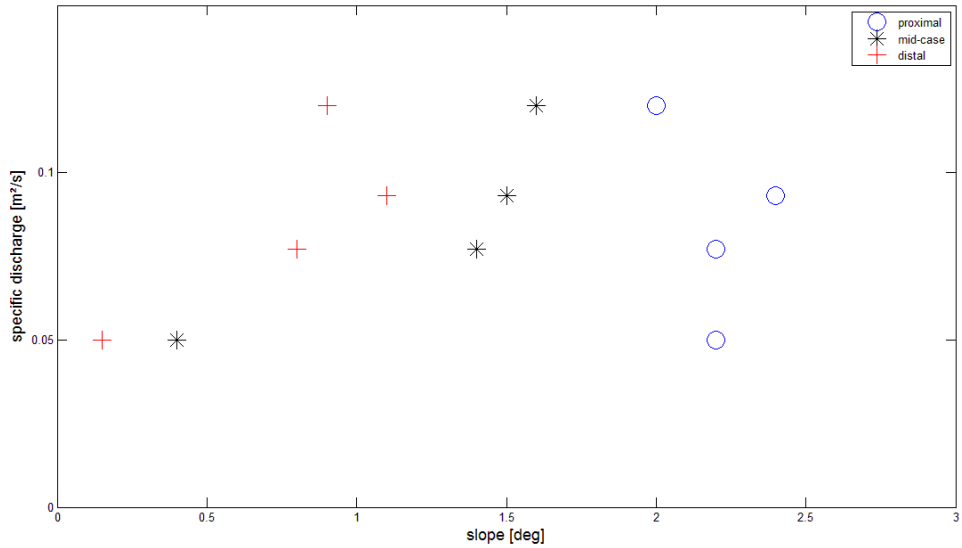

Figure 14: The simulations 1, 2, 4 and 6 all have different specific discharges and other parameters remain the same.

The observed correlation between Froude number ratio and bedform appears to be independent form the discharge. Specific discharges range from 0.05-0.12 m²/s, both end-members display clear, unambiguous cyclic steps, but only as the Fr_{90}/Fr_{50}-ratio becomes lower than a value of roughly 1.6, other bedforms are also stable at a range of varying specific discharges. This pattern is not only observed in the simulations, but also in the physical experiments of Cartigny et al. (2013). Figure 15, clearly illustrates this observation.

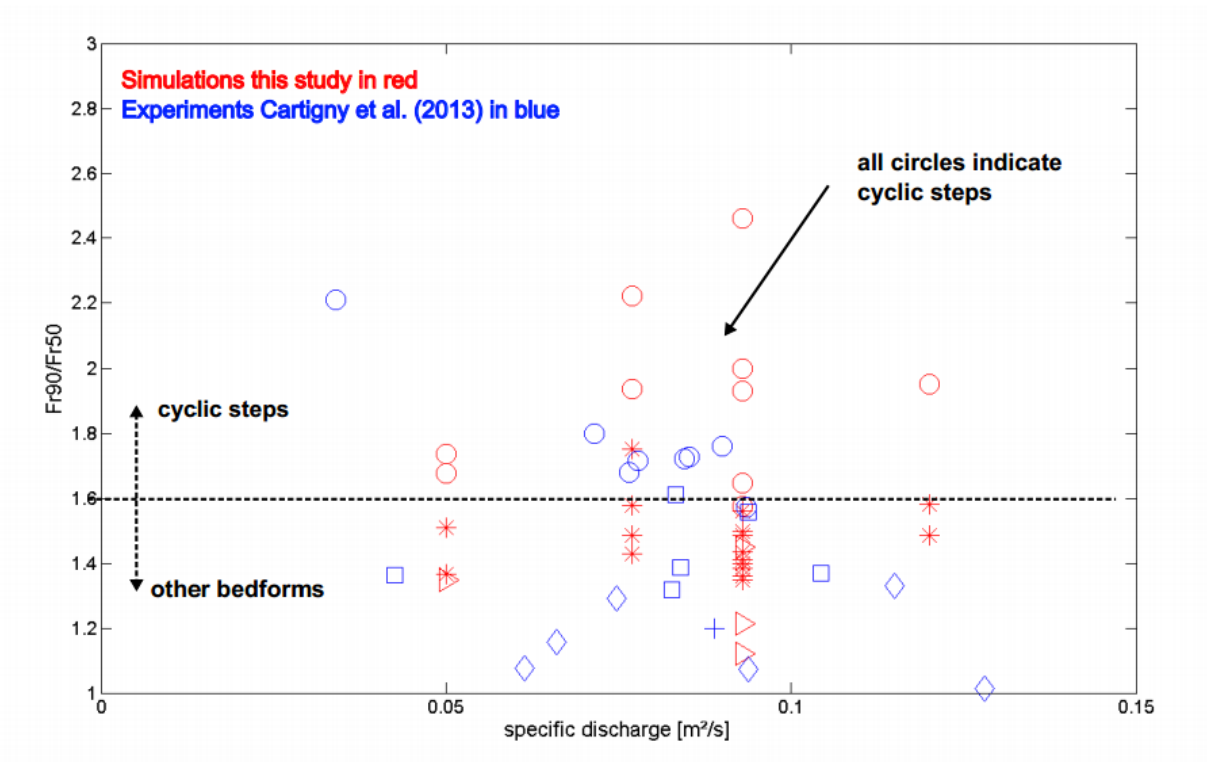

Figure 15: Fr_{90}/Fr_{50}-ratio plotted against specific discharge. The red markers indicate the simulations, the blue ones the experiments of Cartigny et al. (2013). The circles represent cyclic steps, the stars the "undefined" supercritical bedforms observed in the simulations, the squares are a chute-and-pool morphology, the plus-sign represents unstable antidunes, the diamonds regular antidunes and the triangles indicate a flat-bed without bedforms.

Sediment concentration effects

The second independent variable which has been investigated is the sediment concentration of inflowing water-sediment-mixture.

The inlet-sediment concentration is poorly constrained in the physical experiment, because recirculating flume tanks were used in the experiments of Alexander et al. (2001) and Cartigny et al. (2013). Such a recirculating aspect of the physical model was not simulated, a sediment concentration of 150kg/m³ (~5.7 vol %) is used because it appears to be a realistic sediment concentration and, does appear to lead to a stable, roughly transportational system. The effect of the sediment concentration has been studied by changing the sediment inflow concentration to 75kg/m³, 175kg/m³ and 250kg/m³ as simulations 1, 3, 5a and 5b are compared (figure 16).

In case of 5a, the sediment concentration at the Xmin boundary is set to 250kg/m³, the amount of sediment deposited at the model entrance is so large, the inlet is "plugged". There seems to be a correlation between the slope and the availability of sediment on the Xmin boundary. Higher concentrations of sediment lead to a higher slope, proximal as well as more distal.

The investigated concentration of sediment in the inflow concentrations investigated appears to have little effect on the developed bedforms. In all instances, undefined supercritical bedforms are formed at $Fr_{90}/Fr_{50}<1.6$ and cyclic steps at $Fr_{90}/Fr_{50}>1.6$.

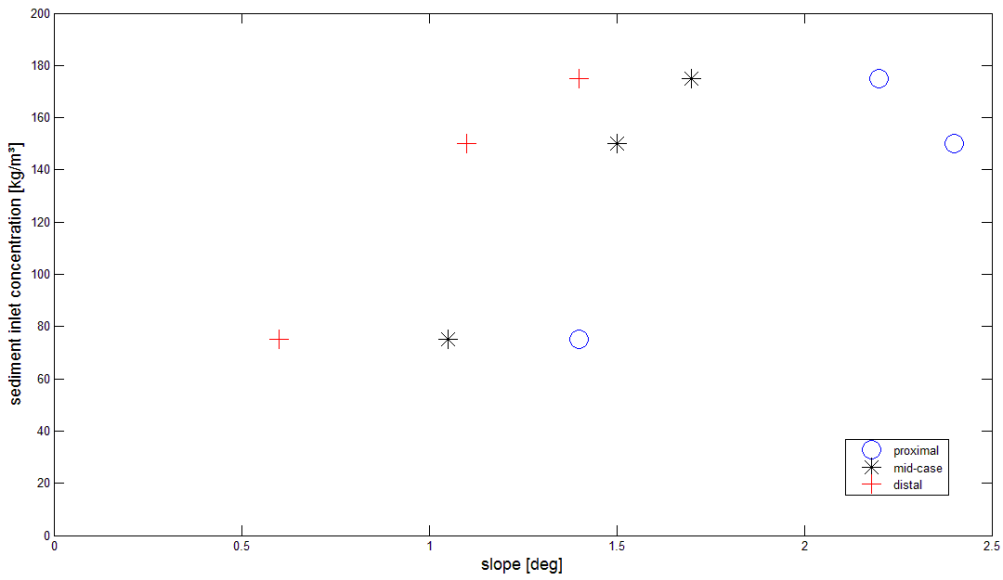

Figure 16: Sediment concentration at the inlet plotted against the developed mean slope. Three identical simulations with only sediment concentration changed in the inlet are displayed (75,150 and 175 kg/m³).

Grain size effects

The third tested independent variable is the size of the spherical quartz-grains used in the simulation. Four different mono-disperse grain-sizes have been tested in the model. (160, 265, 350 and 450 µm in diameter); in simulations 1, 7, 8 and 9. The inlet conditions of simulation 1 are maintained (0.093m²/s with 150kg/m³ of sediment).

In case of the 160µm fine sand run, there is a lot of scour at the model inflow. No slope is developed and the bed remains smooth. Median and 90th percentile Froude numbers and flow velocities are not far apart. There are some oscillations in the flow-depth, the flow regime generally remained subcritical but near critical conditions. The first 300 seconds of the simulation major erosion of the

pre-existing 160µm occurs, an equilibrium is then reached at which a net-transportational, smooth bed is present.

The 265µm medium sand run resulted in stronger scour at the flume entrance than in the 350µm case. In contrast to the fine sand however, a slope is able to develop. The slope proximally is smaller than in simulation 1 (1.7°) but similar more distally. The bedforms that populate on the slope are similar to the ones found in the 350µm base-case, Froude numbers, velocity medians and 90th percentile are also similar. No clear distinction in bedform shape between the 265µm and 350µm can be observed.

A coarsening of the grain size to 450µm, leads to proximal steepening of the slope. Bedforms, Froude number ratios and velocities are similar to those in simulations 1 and 8 (350µm and 265µm). Bedform morphology and migration speeds appear not to differ significantly from the base.

Overall it can be said that an increase in grain size, leads to an increase in mean slope, in particular in the proximal parts of the simulation, this can be observed clearly in figure 17. In simulations the effect of grain size appears to be absent for larger grain sizes, but the smaller 160µm sand does yield a different morphology, a flatbed (figure 17b). In the physical experiments however this is not observed.

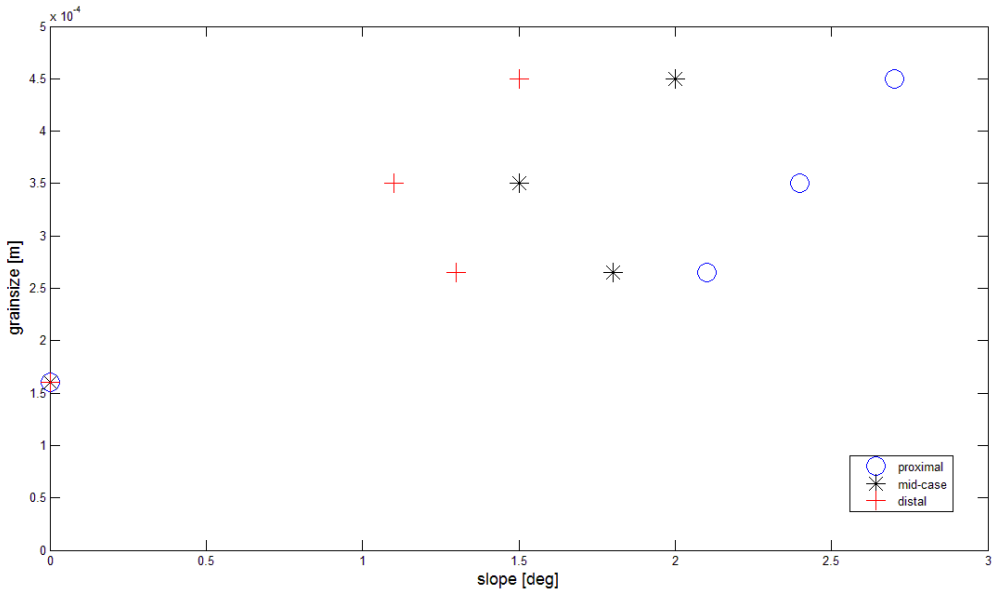

Figure 17: slope plotted against grain size of the simulations in which all other parameters but grain size remained constant.

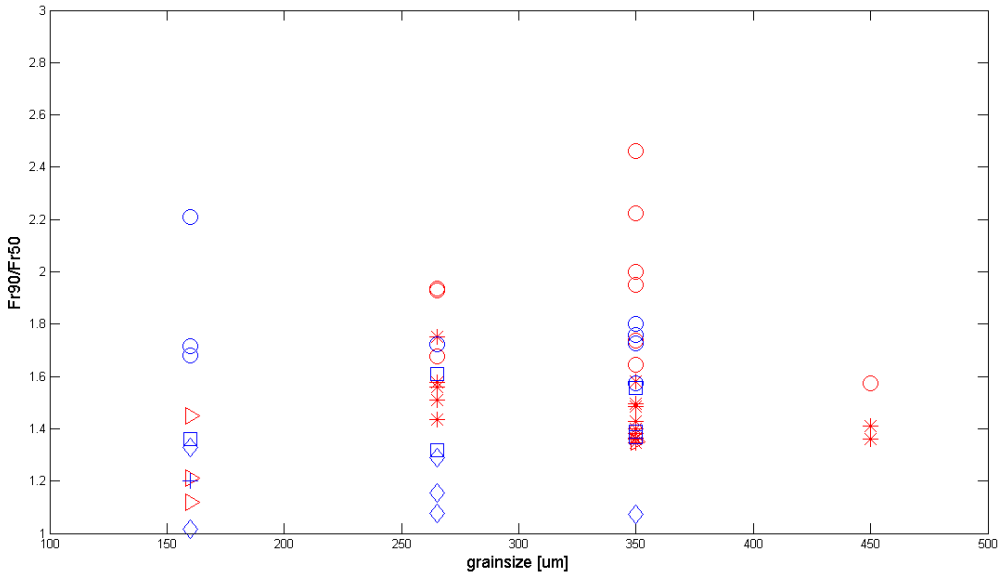

Figure 17b: Fr_{90}/Fr_{50}-ratio plotted against grain size. The red markers indicate the simulations, the blue ones the experiments of Cartigny et al. (2013). The circles represent cyclic steps, the stars the "undefined" supercritical bedforms observed in the simulations, the squares are a chute-and-pool morphology, the plus-sign represents breaking antidunes, the diamonds regular antidunes and the triangles indicate a flat-bed without bedforms.

Flow-dynamics and bed-interaction over cyclic steps

To gain further insights in the mechanics of the supercritical-flow bedforms and the associated flow, depth resolved properties as the velocity field, sediment concentrations and shear stresses in relation to the bed-morphology are discussed in this section.

Velocity structure and flow-regime

The velocity profiles are based on a time-series at a stationary location whilst an upstream-migrating cyclic step passes by. The velocity structure is analysed at five profile locations constructed from the time series, figure 18. A snap-shot of the flow over a cyclic step is also shown in figure 19.

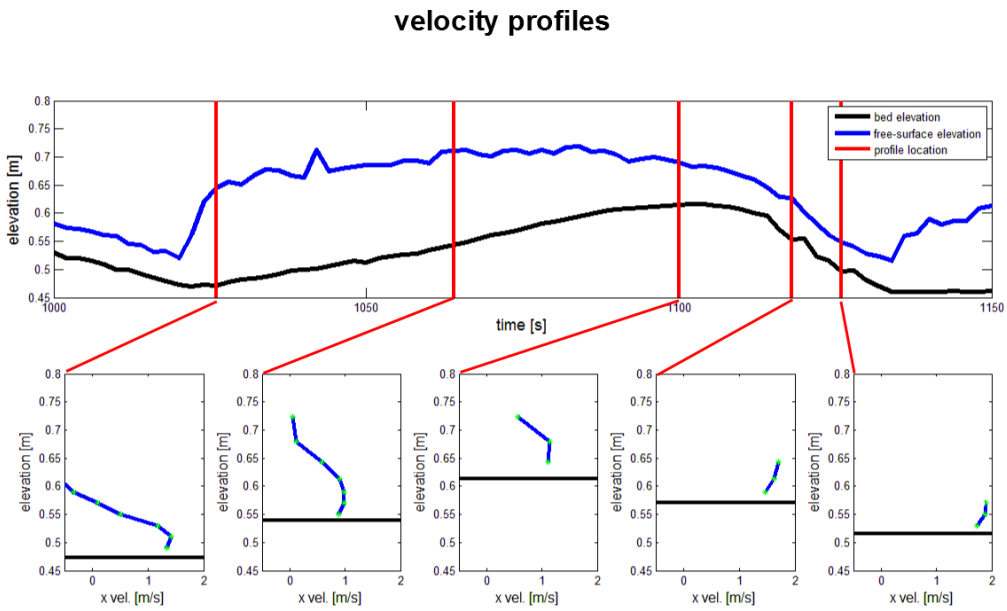

Figure 18: a time-series sequence of 150 seconds taken at the same location x=2m, five velocity profiles have been constructed.

On the stoss-side of the cyclic-step a thick, subcritical flow is present, the 2nd velocity profile in figure 18 represents this. Flow-velocities reach up to about 1m/s near the bottom of the flow and decrease gradually towards the top; not a velocity structure from what would be expected of open-channel flows. As the flow approaches the crest of the cyclic step, the flow thins and accelerates towards near-critical Froude numbers and, starts to normalize its velocity structure as seen clearly in profile 3 of figure 18. At the lee-side of the bedform, further acceleration and thinning of the flow is observed, causing it to become supercritical. Flow velocities reach speeds up to about 2m/s, in figure 19 and profile 4 of figure 18 it can clearly be seen that the flow-structure has normalized to one in which highest velocities are reached near the free-surface, for some reason this cannot be seen clearly in profile 5, possibly due to a numerical artefact in the top-cell. When the flow reaches the lee-side of the cyclic step again, it decelerates rapidly and creates a hydraulic jump. At the hydraulic jump, the velocity structure displays the largest anomaly from what would be expected of open channel flows. The top part of the flow is strongly affected by rollers created by the hydraulic jump, making negative x-velocities possible, negative x-velocities imply a flow upstream, these negative velocities are observed clearly in profile 1 of figure 18, but can also be observed in figure 19, rollers and vortices usually develop on top of the flow but there are periods in which they form below the main flow. The lower half of the flow keeps a downstream-directed flow vector of about 1 to 1.5 m/s. The effect of the roller with negative velocities is observed over almost the entire stoss-side of the cyclic step, in

which velocity profiles are not what would be expected of regular open-channel flows, it is only at the lee-side that the velocity-structure is completely normal again.

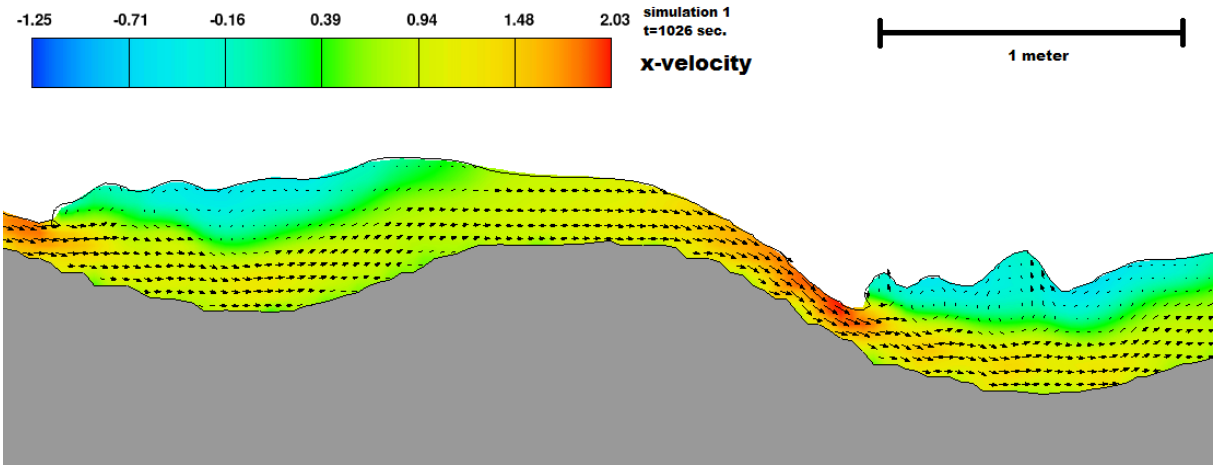

Figure 19: A snapshot of a cyclic step in simulation one, around x=2-4.5m at t=1026 seconds. The y-axis is exaggerated by 200% with respect to the x-axis. The x-vector of the flow-velocity is displayed in colour gradients.

The Froude numbers in the flow change from subcritical at the stoss-side following a hydraulic jump, to supercritical at the lee side (figure 20). Hydraulic theory dictates that flows are critical over a weir, and one might think the same applies to the crest of a cyclic step. The Froude number at the crest of a cyclic step in the simulation is however 1.22 on average (sample size of 29 cyclic steps; standard deviation of 0.15).

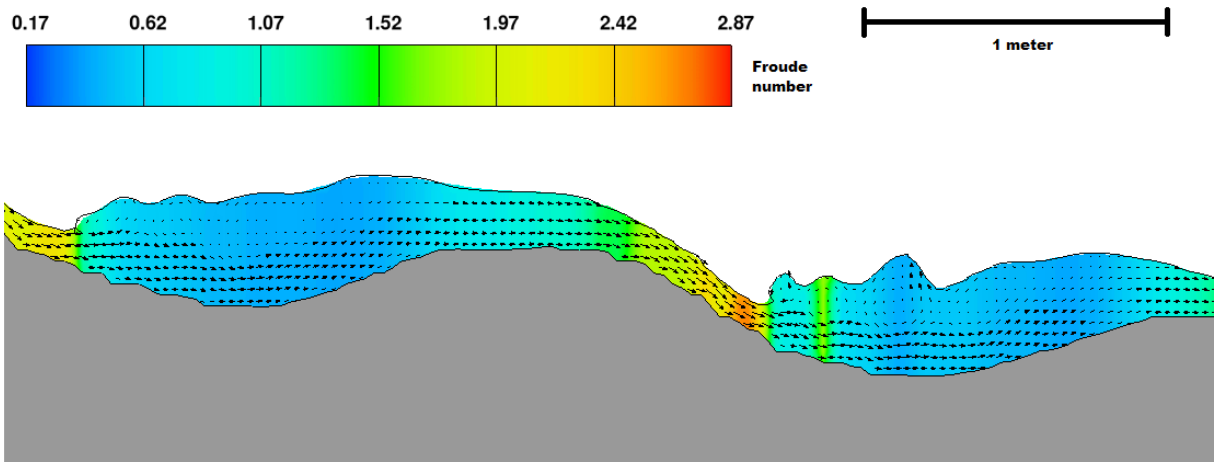

Figure 20: A snapshot of a cyclic step in simulation one, around x=2-4.5m at t=1026 seconds. The y-axis is exaggerated by 200% with respect to the x-axis. The Froude number is displayed in colour gradients.

Shear stresses

The "excess shear stress" is a dimensionless number representing the excess shear stress exerted by the flow on the bed, it actually is (Θ_i - Θ_{cr}); the local Shields number minus the critical Shields number, so "excess Shields number" might have been a more clear term, for the sake of uniformity however the term excess shear stress will be used. Both the shear velocity and the dynamic viscosity,

which is turbulence dependent, affect the shear stress. As seen in figure 21 the dynamic viscosity is largely increased by the vortices in the hydraulic jump, the effect near the bed boundary layer is quite small. In figure 22 the median excess shear stress on the bed is visualized, the irregular character of the graph is a result of the sometimes strong peaks and irregular character of shear stress, even after averaging over 12 cyclic steps, high-shear-stress periods of some cyclic steps remain visible. The overall shear-stress-pattern over the crest of a cyclic step shows a gradual increase of the excess shear stress from around 5 to about 10-15. The excess shear stress gradually drops to less than 5 over the hydraulic jump. It is important to note that excess shear stresses can exceed the mean, ~12 in the supercritical flow, 2 to 4 times at short time steps (as seen in figure 23), it is yet unclear whether this is a numerical artefact or these stresses are realistic, for that reason the median excess shear stress has been used instead of the mean excess shear stress; to filter out these high peaks of individual cyclic steps.

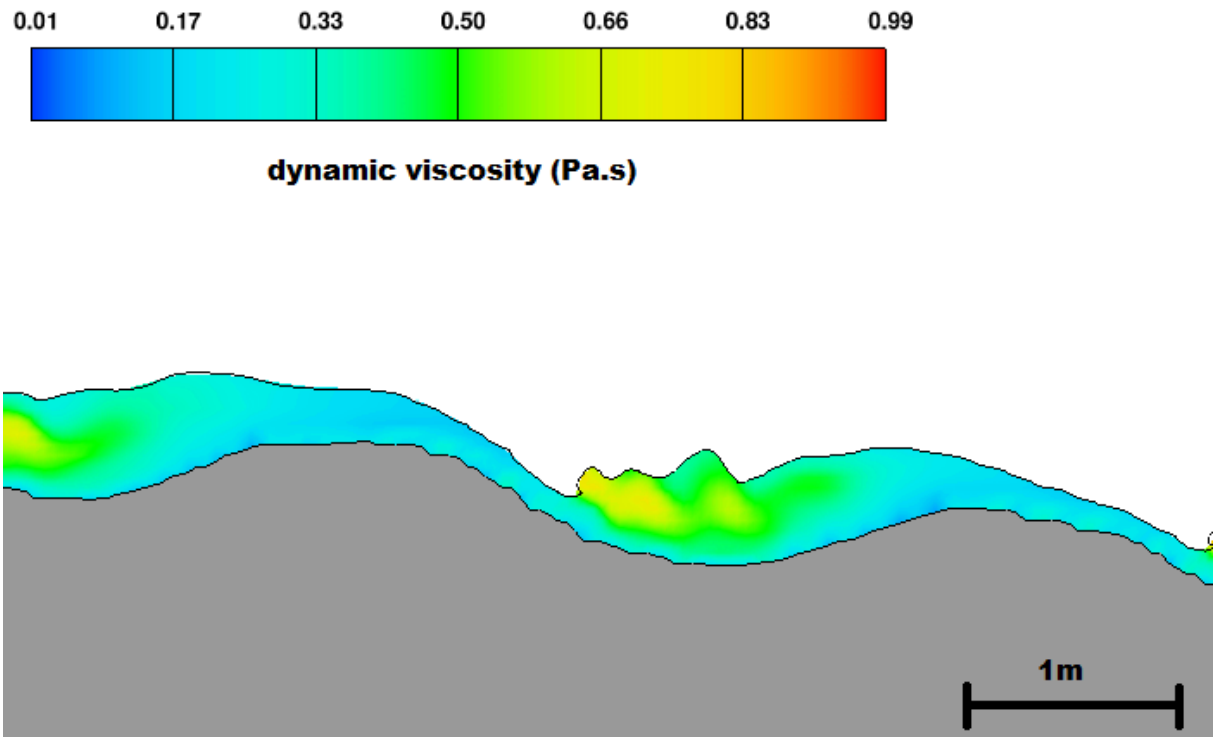

Figure 21: the dynamic viscosity of a flow over a cyclic step. Highest viscosities are observed in high-turbulence roller and vortex structures.

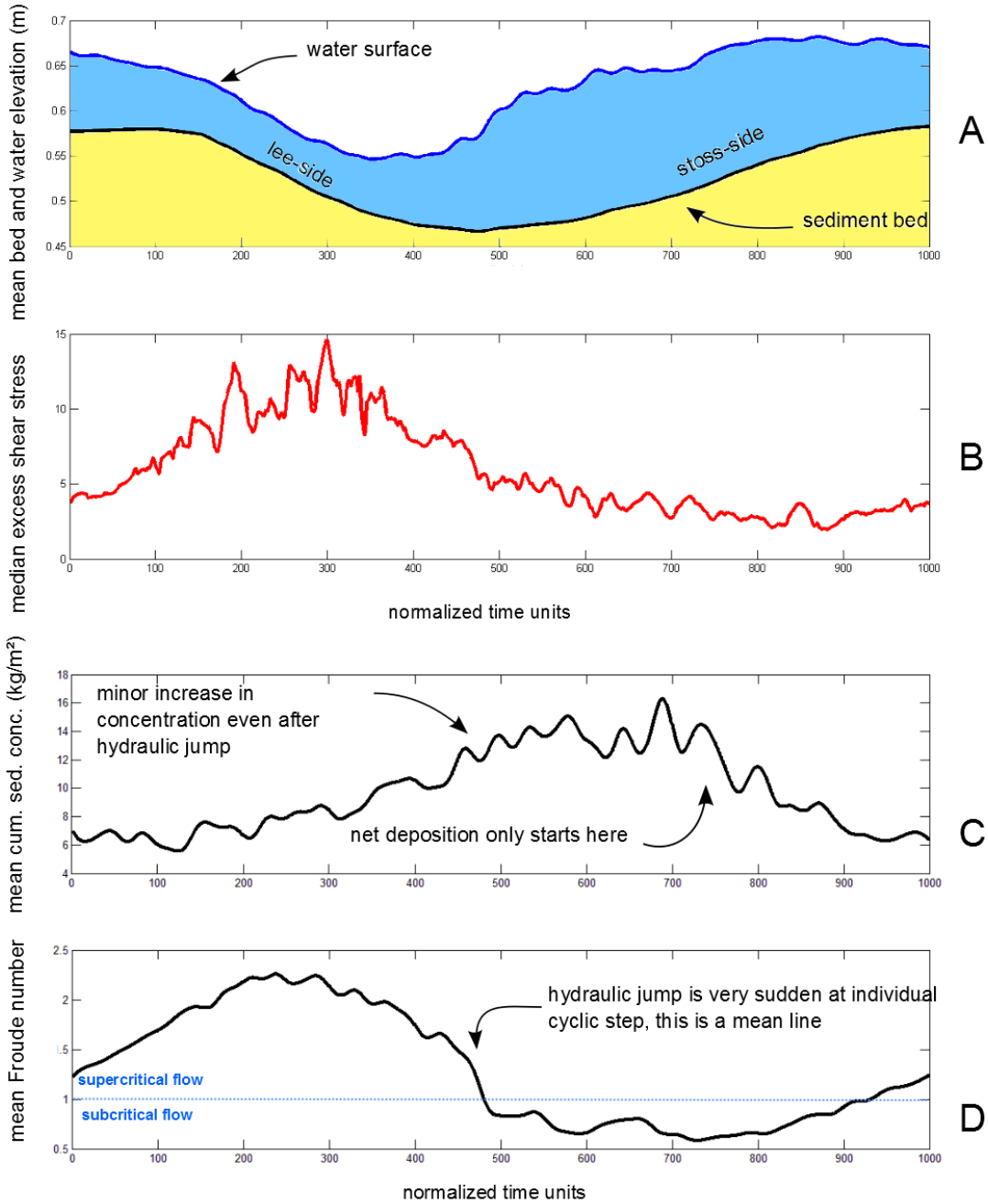

Figure 22: Averaged values of sediment height (A in black), free-surface elevation (A in blue), excess shear stress (B), cumulative sediment concentration (C) and mean Froude number (D) of 29 cyclic steps (simulation 1) obtained via a time-series (fixed location).

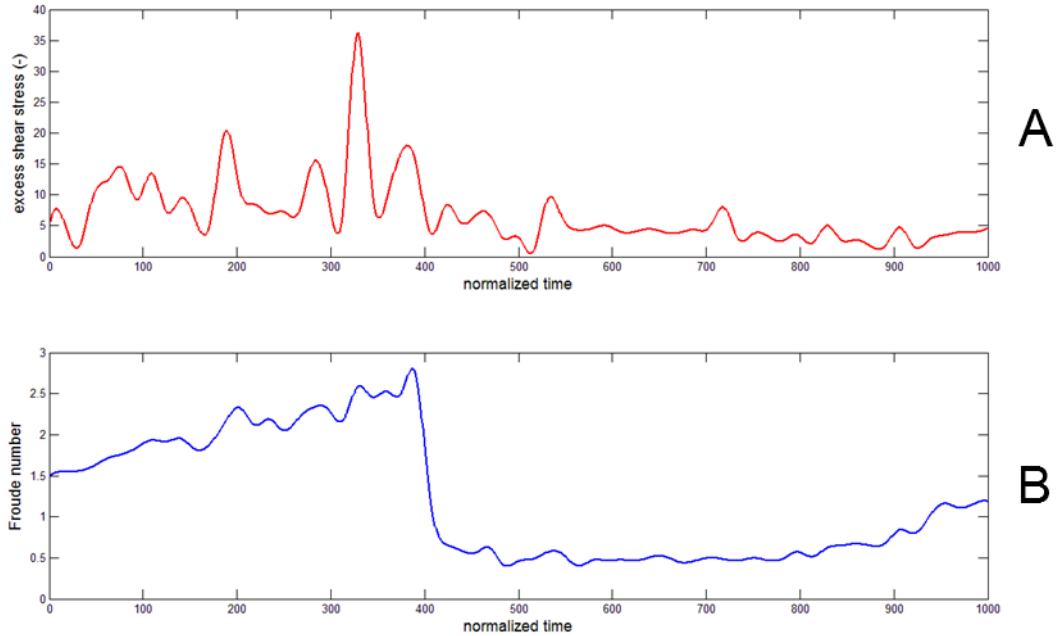

Figure: 23: The excess shear stress on the bed (A) and Froude number of the flow (B) of one individual cyclic step.

Suspended sediment concentration

The suspended sediment concentration is difficult to measure in flume experiments, depth-averaged numerical simulations are also unable to provide insights in the distribution of sediment over the water column. Profiles of suspended sediment concentration have been constructed at the same time intervals as the velocity profiles (figure 24). A snap-shot in time of suspended sediment concentration over a cyclic step is seen in figure 25.

The concentration of suspended sediment is highly variable with depth, this becomes particularly clear in profiles in the subcritical flow regime; profiles 1 and 2, in which it is visible that there is no sediment in the top-layer of the flow. Concentrations reach values 200-300 kg/m³ (=8-11 vol %) near the bed. In figure 25 it can be seen that at certain locations; in particular near the bed in the through of a cyclic step, concentration can exceed 500kg/m³. As the fluid becomes supercritical over the crest of the cyclic step, the concentration remains highest at the bottom layer at about 200kg/m³ and near-zero at the top of the flow.

The cumulative amount of sediment in the flow can be observed in figure 22. The amount of sediment in the flow is about 7 kg/m² when the flow reaches the crest, and gradually increases towards about 14 kg/m² at 500 normalized time units. The cumulative sediment mass in a column remains around this value some time until the amount of sediment suspended in the water drops relatively quickly around 750 normalized time units. Values around 7 kg/m² are reached again as the top of the crest is reached.

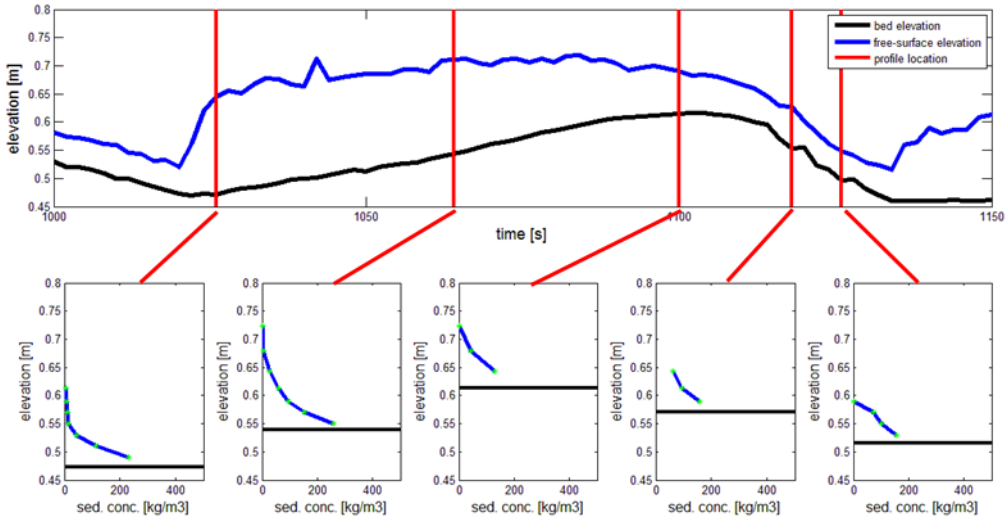

Figure 24: five profiles of suspended sediment concentration over time at location x=2m.

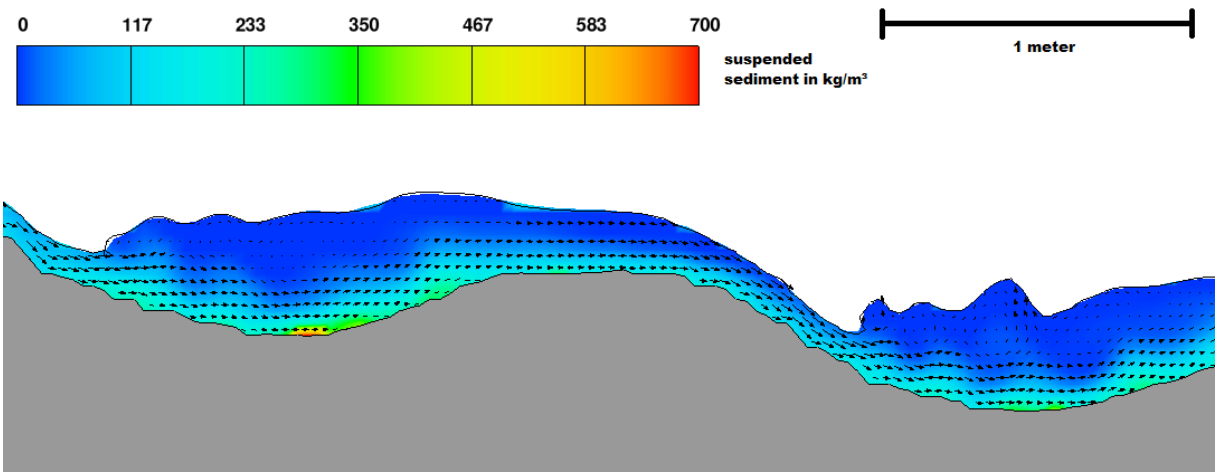

Figure 25: A snapshot of a cyclic step in simulation one, around x=2-4.5m at t=1026 seconds. The y-axis is exaggerated by 200% with respect to the x-axis. The colour gradients display the concentration of suspended sediment.

Erosion and deposition patterns

The patterns of erosion and deposition in simulation 1 have been visualised in figure 26. The cyclic step migrates upstream due to erosion on the lee-side and deposition on the stoss-side. The rate of erosion and deposition causes a period of migration of around 115 seconds for the cyclic steps. The areas in which erosion takes place correspond with the high-shear-stress supercritical lee-sides of the flow over the cyclic step. Deposition occurs at the predominantly subcritical lee-side where low-shear-stresses are observed in figure 22 as well.

Although all cyclic steps show similar behaviour, their geometry over time can be somewhat variable figure 27 displays the variance in geometry of cyclic steps over time. The general internal structure of a cyclic step bedform is that of horizontal to low-angle backset lamination (more down current), cut off at a relatively high (up to 20 degrees) on down current side. The upstream first third of the stoss

side shows almost no deposits, the second third shows a relatively horizontal lamination increasing in thickness, and the third of the stoss-side of a cyclic steps show low-angle backset lamination of more-or-less constant thickness (figure 26).

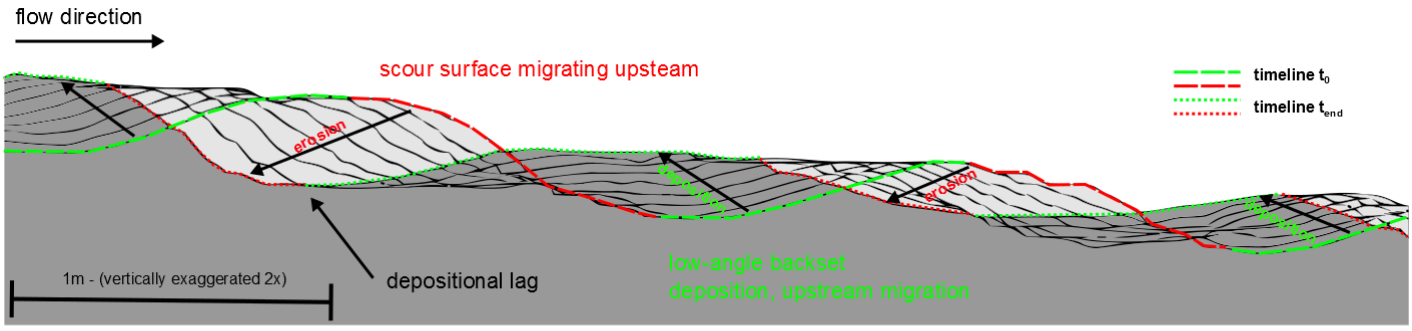

Figure 26: the deposition and erosion structure at a cyclic step: the laminations are drawn in every 8 seconds.

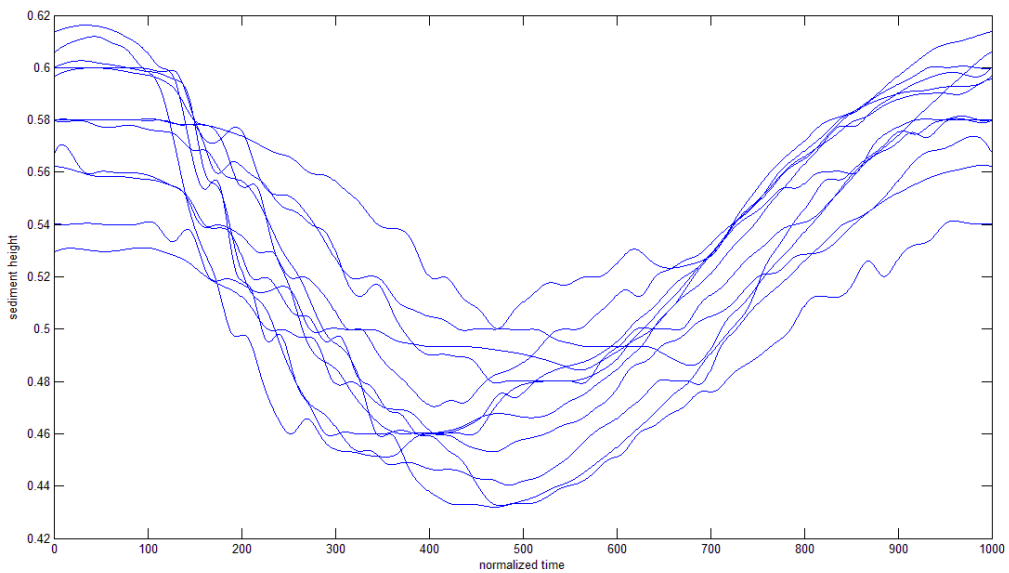

Figure 27: normalized time-series analysis of 29 cyclic steps of simulation 1 showing the variability in cyclic step morphology.

Results: turbidity currents

An attempt has been made to model supercritical-flow bedforms in turbidity current settings. The experiments of Jorritsma (1973) are used as reference, because these experiments have shown to produce cyclic steps in turbidity current settings. Although no clear cyclic steps formed during the numerical simulations, some hydraulic jumps in turbidity currents have been observed. The hydraulic jumps remained stable for periods of ~250 seconds. Undulating bedforms have also been observed in the numerical simulations. In contrast to the free-surface flow bedforms, the turbidity current bedforms were purely depositional, lacking erosion on lee-sides. The crest of the bedforms however does migrate upstream while the bed aggrades. Although little data is available to assess equilibrium conditions on specific bedforms equilibrium condition, the flow-properties over supercritical-flow bedform can be investigated.

Flow-dynamics and bed-interaction of supercritical turbidity currents

Velocity structure and flow regime

The modelled turbidity current has an averaged flow thickness of about 20 cm. Although it should be kept in mind that the definition of thickness of the flow is somewhat arbitrary. The first velocity profile of the turbidity current is located at x=9.5 m, at the crest of a bedform. The velocity structure is what one would expect from a turbidity current, with highest flow velocities near the bottom (reaching up to about 0.9 m/s), the flow velocity gradually decreases towards the top of the current. The second velocity profile is located at the lee-side of a bedform, flow velocities have increased slightly as observed in figure 28; the maximum flow velocity reaches about 1 m/s near the bed. Between 11m and 12m on the x-axis a hydraulic jump is visible, a profile near the hydraulic jump is the third velocity profile in figure 28. The flow clearly thickens and a roller is developed (which displays near-zero and even negative flow-velocities in the x-direction) in contrast to the free-surface flow, a roller is developed on the bottom of the current, rather than the top. The maximum flow velocity is now near the top of the flow and is still 0.9 m/s, it has not decreased rapidly from before the hydraulic jump. The densimetric Froude number over the hydraulic jump decreases from between 1 and 1.5 before the jump to subcritical at the jump associated with the roller, from about 12.3m onwards, the flow becomes supercritical again according to the depth-averaged method (figure29). When the integral method of Garcia & Parker (1993) is used, the Froude numbers roughly correspond, however, at the hydraulic jump the integral method diverges from the depth averaged method in the way that the flow becomes supercritical on top of the roller again, and experiences a second hydraulic jump before leaving the dense roller-structure

After the hydraulic jump area with the rollers the flow obtains a normal velocity structure again. The maximum velocities are reached near the bed again, at speeds of about 0.7m/s (profile 4 figure 28), this is still slower than the velocity before the hydraulic jump. The last velocity profile is similar to the 4th one, displays a normal velocity structure and is supercritical again as densimetric Froude numbers exceed unity.

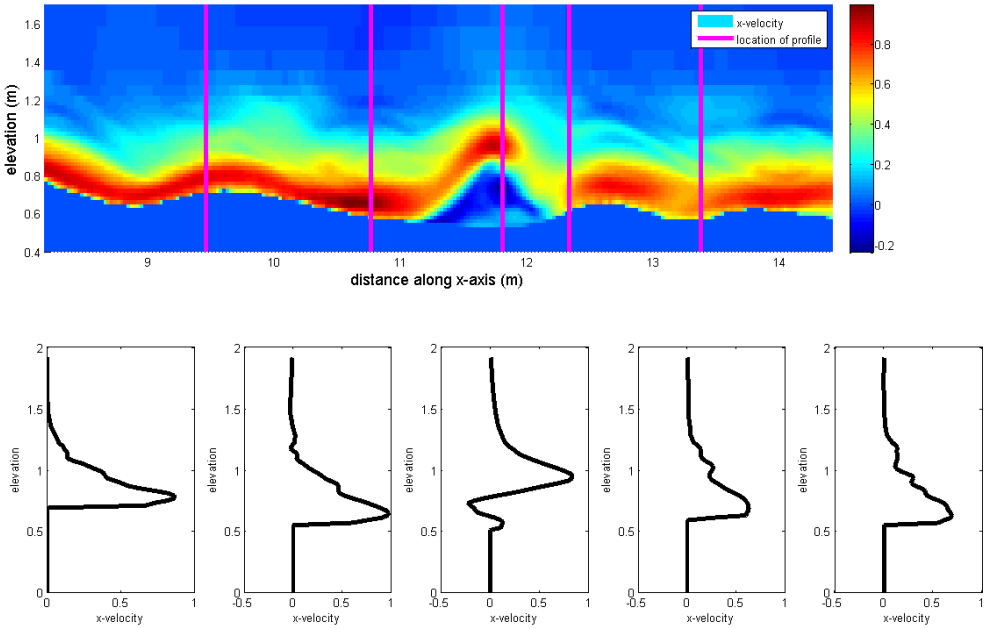

Figure 28: The x-velocities in the turbidity current –indicated by a colour map-, the current flow from left to right. The profile locations are indicated by the pink stripes. The vertical (elevation) is exaggerated by 200%.

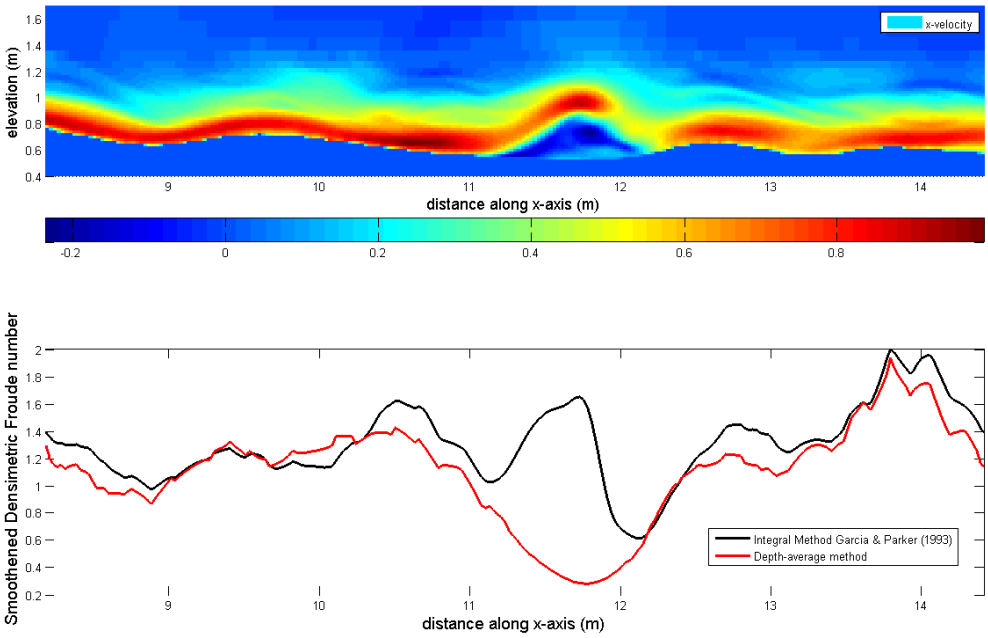

Figure 29: densimetric Froude number over the hydraulic jump in a turbidity current, based on depth-averaged method and the integral approach as proposed by Garcia & Parker, (1993).

Shear stresses

The flow-velocity near the bed is closely related to the shear stress. Excess shear stresses in the simulation are generally about 2-4. A clear peak in excess shear stress can be observed at x=10m a general high shear-stress-zone is located between 10-11m as well, this corresponds with the high velocities observed on the lee-side of the bedform here (figure 30). At the roller of the hydraulic jump flow velocities near the bed are very low, consequently excess shear stresses are near-zero. As the flow velocity near the bed picks up, so are do the shear stresses, there are some clear spikes in excess shear stress.

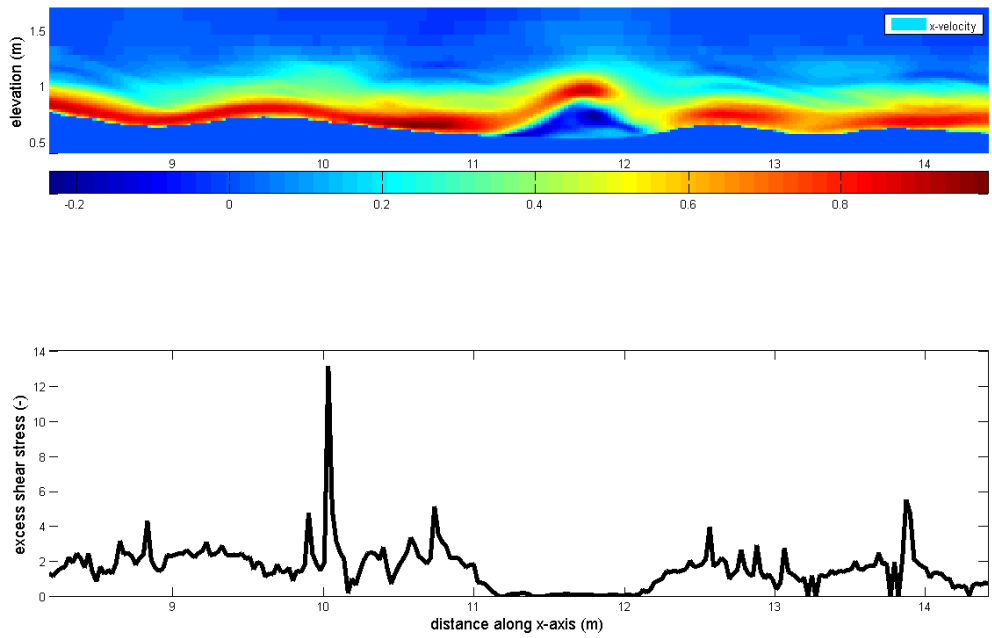

Figure 30: The velocity in colour map and the excess shear stress of the simulation of the turbidity current-case.

Suspended sediment concentration

The concentration of suspended sediment in the turbidity current is analysed and the concentration distribution and profiles can be observed in figure 31. A vast majority of the sediment is suspended within the bottom 20cm in profiles 1, 2, 4 and 5. Before the hydraulic jump in the supercritical flow, the maximum concentration reaches to about 700-800 kg/m³ (~30 vol %) near the bed. At the hydraulic jump the amount of suspended sediment in the low-velocity roller is generally >500kg/m³ (~20 vol%), this is within a thick, high-density layer over which a lower-density high velocity detached flow is present (as seen in the velocity profiles in figure 28) maximum flow velocities are at an elevation of about 1m, where the sediment concentration is very low.

Behind the rollers, a thin, high-concentration basal layer is developed again. The concentrations appear to be somewhat higher than before the hydraulic jump, this is seen in the profiles as well as by the darker reds seen in the 2D figure.

The depth-integrated sediment concentration in the flow is around 30-40kg/m² before and after the hydraulic jump. At the hydraulic jump with associated rollers there is a lot of sediment in suspension resulting in about 180kg/m² in the water column in this region (figure 32).

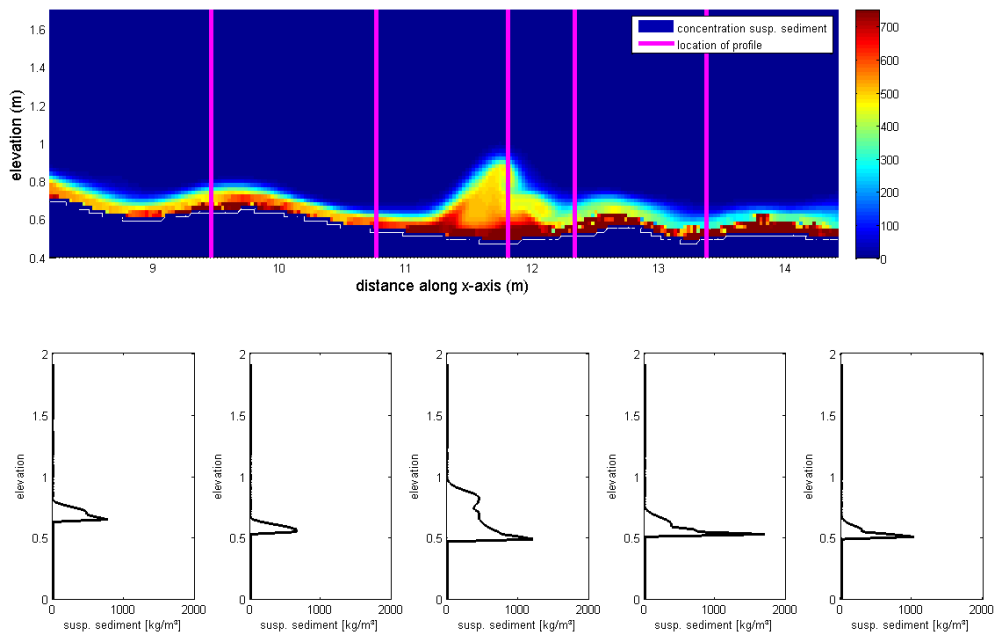

Figure 31: The amount of suspended sediment in the simulated turbidity current, concentrations are in kg/m³. The same location and time-step is seen as in the velocity and shear-stress- analysis.

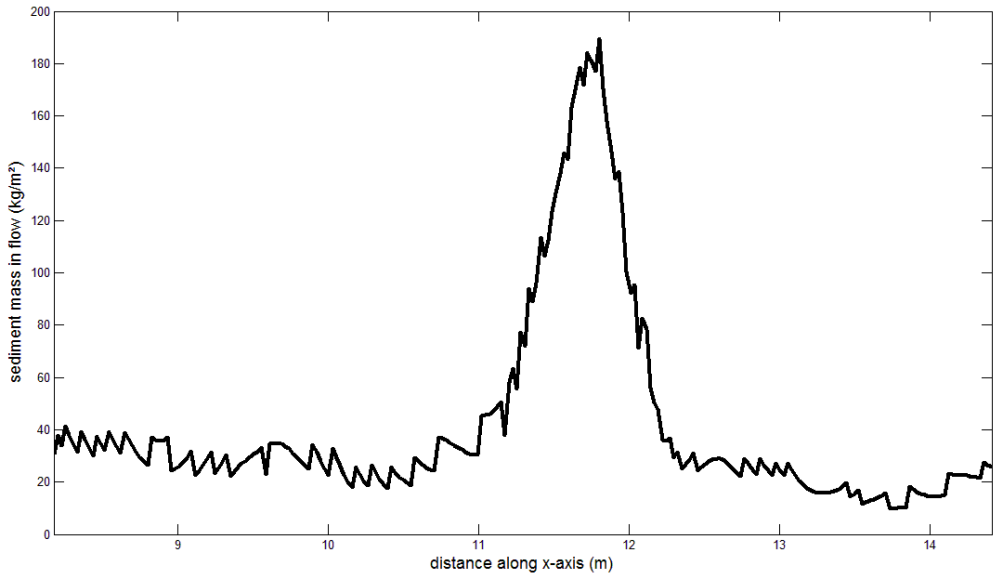

Figure 32: depth-integrated sediment mass in the turbidity current flow per meter over the flow height and cell-distance

Erosion and deposition patterns

The simulation of the turbidity current was purely depositional. A few trends can however be observed. At the high-velocity lee-side of the first bedform in figure 33, there is almost no deposition, the depocenter is located at the low-velocity region just after the hydraulic jump, this is also the location where shear stresses are lowest and cumulative sediment mass in suspension is highest. The system as observed in the simulation is aggradational and shows a slight upstream migration of the crests of the identified bedforms, as indicated by the orange arrow in figure 33.

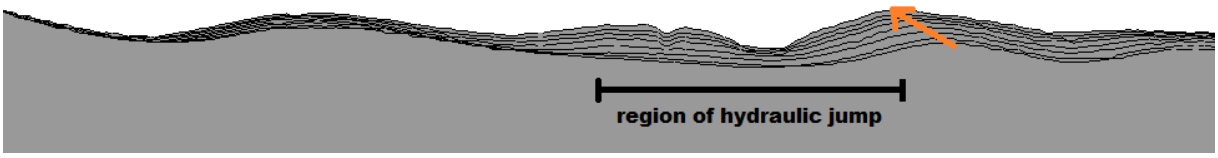

Figure 33: the internal structure of the deposits in the simulation of a turbidity current with hydraulic jump.

Discussion

Model validity

The results show that FLOW-3D® is capable of simulating cyclic steps in a free-surface open-channel flow. The rates of bedform migration, bed geometries and flow-properties correspond closely with the physical experiments of for example Cartigny et al. (2013). The display of continuous hydraulic jumps at these bedforms unambiguously defines them as cyclic steps, the hydraulic jumps display multiple vortices and rollers capable of generating negative x-directed velocities, which is often seen in hydraulics (Long et al. 1991). The continuous hydraulic jumps also cause a relatively high Fr_{90}/Fr_{50} numbers, exceeding 1.6, these values are similar to those observed in the physical experiments. The upstream migrating cyclic steps in the simulation migrate with a period of 118 seconds on average, this is within the 80-120 second range as described by Cartigny et al. (2013).

Although some of the simulations which should yield antidunes according to the physical experiments and relationships of Kennedy (1960), Kennedy (1961), Alexander et al. (2001) and Cartigny et al. (2013), none of them actually displayed geometries and flow properties consistent with an antidune morphology. One would expect continuously supercritical flow, associated with standing waves and with Fr_{90} and Fr_{50} closely together (ratio <1.2). Antidune wavelengths are expected to be smaller (~1.4m) than those observed in the simulations (2.1m and 1.7m on average for mid-cases and distal cases respectively). Antidunes may be a result of free-surface standing wave undulations (Kennedy, 1960; Grand, 1997; Chanson, 2000), though not necessarily at critical flow conditions (Chanson, 2000). If antidunes truly are formed as a result of free-surface undulations, standing waves, it is unlikely that antidunes can be formed in the model, as the governing process may not be captured within the model.

The process that has been observed when antidunes should be formed is one of supercritical flow over the bed, creating a bedform at first, after tens of seconds however the bedforms oversteepen, a free-surface wave and a hydraulic jump surge migrates upstream. The undefined supercritical bedforms themselves also migrate upstream with a 130-140 second period, these rates of migration clearly do not correspond with those of chutes-and-pools or unstable antidunes both at 200-250 seconds, nor stable antidunes at ~60 seconds (Cartigny et al., 2013). In terms of hydraulic parameters - especially Fr_{90}/Fr_{50} - the bedforms closest resemble a chute-and-pool morphology at ratios of 1.3-1.6, this can also be observed in figure 15. Because the antidune formation process is possibly not captured in FLOW-3D®, the bedforms observed might be ones that would normally not be observed in the physical world, the process responsible for the creation of the (unstable) antidunes and chutes-and-pools in the physical world would likely overrule the process responsible for the creation of these undefined supercritical bedforms as observed in the simulations.

Parker & Izumi (200), Sun & Parker (2005) and Balmforth & Vakil (2012), whom simulated cyclic steps using depth-averaging methods, suggest they are caused by “interaction between the flow dynamics and the erodible bed, and are expected once the flow becomes supercritical” (Balmforth & Vakil, 2012). Although the simulations performed in this study did not yield cyclic steps at every supercritical flow, an instability creating hydraulic jumps - though not continuous as required for cyclic steps - is observed. The reason for the difference in response of the bed on the supercritical flow between the depth-averaged models and this depth-resolved model is not completely clear at this point. The character of cyclic steps developing as soon as flow becomes supercritical is not seen in experiments, in which a multitude of other supercritical-flow bedforms formed at lower supercritical Froude numbers can be formed.

Equilibrium conditions for bedforms

Independent variables; specific discharge, inlet sediment concentration and grain size have been varied in the simulations to assess their influence on the stability and equilibrium conditions at which bedforms in free-surface supercritical flow are created.

The bedforms that have been observed in the simulations are (1) cyclic steps, (2) the undefined supercritical bedforms and (3) a (upper stage) plane bed. The cyclic steps have predominantly been formed in the relatively high-slope proximal areas of the simulations. In figure 12 it can be seen that both Fr_{90}/Fr_{50} and slope correlate well with the type of bedform. Slopes exceeding approximately 2 degrees as well as Fr_{90}/Fr_{50}-ratios exceeding 1.6 in almost all cases yield cyclic steps. In figure 15 it can be seen that the correlation of Fr_{90}/Fr_{50}-ratio to bedform does not only hold for numerical simulations, but also for the physical experiments of Cartigny et al. (2013), unfortunately other authors do not provide both Froude-numbers to further extend this database, the amount of data points is however large enough to observe this trend.

The mobility parameter (Θ_{90}) of Van den Berg & Van Gelder (1993) may show some correlation with observed bedform for the physical experiments of Cartigny et al. (2013) (see figure 13), but fails to provide a clear pattern in the simulations. Θ_{90}-values in the simulations are consistently much lower than those in the experiments, they never exceed 2.3 whereas values up to 9 may be reached in similar experimental settings. A cause for this may be that a mono-disperse grain size is used in the simulations; this means $D_{50}=D_{90}$. Both D_{50} and D_{90} (via the 90th percentile Chézy coefficient in equation 5.2) are needed in the calculation of the Froude number. A low D_{90} leads to low Chézy coefficients and thus also a lower mobility parameter (equation 5.1 and 5.2). The effect of the mono-disparity of the grains however is only minimal and would lead to an increase of about 0.5 (25%) if $D_{90}=2D_{50}$. The u_{90} and h_{10} appear to have a more profound effect on the Θ_{90}, as they are squared. If h_{10} is higher and u_{90} is lower, the Θ_{90} will be significantly lower too. It may well be the case that the sediment transport coefficients; bed-load coefficient and entrainment coefficient, are too high within the simulations. The high coefficients within the model would lead to the situation in which the same sediment transport, resulting in the same morphological signature, is reached at lower peak flow-velocities (u_{90}) and higher flow depths (h_{10}), indicated by a lower mobility parameter than would be expected. A contradicting aspect to this theory however is the observation that in general the Fr_{90}/Fr_{50}-ratios of the simulations are higher than those of the physical experiments, suggesting the exact opposite situation, a higher u_{90} and lower h_{10} in the simulations.

The effect of discharge on slope clearly is that an increased specific discharge generally increases the equilibrium slope (figure 14). An increase in discharge increases sediment supply, as concentration is not changed, more sediment consequently leads to higher rates of sediment fallout (deposits). A similar effect is observed as the inlet sediment concentration is changed (figure 16); enhanced sediment availability and deposition leads to higher slopes. The increase in sediment entrainment due to a higher slope is of a lesser effect than the increase of sediment availability and a higher equilibrium slope is reached as a consequence. The equations governing sediment entrainment and bed-load transport (3.8 and 3.9) are not in linear relation with sediment concentration, slope or discharge. The dynamic viscosity which mainly is a result of turbulence and shear velocity, is affected by the slope. Higher slopes will create higher velocities and thinner flows, thus creating higher shear velocities, the flow will also likely become more turbulent as more energy is available to the system, this will ultimately lead to higher shear stresses via equation 3.7. The effect of slope on shear stress also means the sediment entrainment is increased with an increased slope, but apparently not enough to keep the equilibrium slope the same at different discharges or sediment concentrations.

The effect of grain size on the slope is that larger grains are able to maintain higher mean equilibrium slopes. In nature coarser-grained systems are usually associated with higher slopes than fine-grained alluvial systems (Orton & Reading, 1993). Taking into account equation 3.6 an increased grain size diameter reduces the local Shields number and thus sediment entrainment given all other factors remain the same, a higher shear stress is needed to reach the same Shield number, consequently higher slopes can be maintained if the grain size is larger.

Mean equilibrium slopes are not provided in physical experiments so these observations from the simulations cannot be verified by experimental data. Fagerazzi & Sun (2003) and Sun & Parker (2005) however provide some information on slope stability conditions of cyclic steps in depth-averaged simulations. The simulations of Fagerazzi & Sun (2005) were done at slopes between 2.7 and 4.5^{o}, but no further analysis on the slope appears to be done, the depth-resolved simulations of this study suggest cyclic steps are generally formed at slopes exceeding approximately 2 degrees. Sun & Parker (2005), provides an interesting relation between Froude numbers and slopes associated with transportational cyclic step stability. If S_r (=S_e/S_n); the ratio of equilibrium average bed slope in presence of cyclic steps (S_e) to their absence (S_n), is less than unity, the amount of sediment transported (and water discharged) can be maintained at a lower average bed slope with cyclic steps than without them. In other words; when S_r<1 cyclic steps increase sediment transport efficiency. The increase in transport efficiency caused by cyclic steps at a certain slope is determined by two opposing effects (1) the increase of sediment transport capacity by continuously going from an subcritical- to supercritical-flow regime, associated with cyclic steps and (2) the loss of energy in hydraulic jumps decreasing the transport efficiency (Sun & Parker, 2005). Combining Sun & Parker (2005)'s theory with the observation from the depth-resolved simulation; an increase in sediment discharge or grain-size, increases the S_e (equilibrium slope in presence of cyclic steps) due to the shear-stress to slope-relation described in the previous paragraph, the slope at which cyclic steps become a more efficient way to transport sediment also increases and S_r=1 is reached at higher slopes.

The predicted S_r is a function of the Froude number that a normal flow would have before cyclic step development (Fr_n>1 in case of cyclic steps), and the Froude number associated with the threshold of bed erosion (Fr_t<1 in case of cyclic steps) (Sun & Parker, 2005). Fr_n and Fr_t values have not been calculated in this study so a comparison with Sun & Parker (2005) cannot be made in that respect. Slope and Fr_{90}/Fr_{50}-ratio however do correlate; high ratios are associated with high slopes. It is very well possible that high Fr_{90}/Fr_{50}-ratios are a result of a high-slope system. If cyclic steps develop in high slope systems, because the potential energy in the system can be used to develop strong momentum-dominant (Fr>1) flow (or Fr_n>1 in terms of Sun & Parker, 2005), the slope is the actual governing factor of creating the cyclic steps, the Froude-ratio will just be a signature of the morphology and inflow conditions. The increased flow velocities (and hence shear stresses) of higher slopes put a limit on the slope, and are a governing factor on the slope, with again, Froude numbers as a characteristic of the flow. It is important to reiterate that the above statements only apply to the development of cyclic steps and other supercritical-flow bedforms appear first - at lower flow energies - in an overall supercritical regime. This model and the depth-averaged models in literature on cyclic steps however probably not capture the physics of the other bedforms correctly, and hence, their effects on equilibrium conditions are not understood yet.

Flow-dynamics and bed-interaction

An advantage of depth-resolved RANS-modelling over depth-average modelling is that the flow properties can be analysed at different depths in the flow. The velocity structure, shear stresses and concentration of suspended sediment will be related to the morphodynamics of cyclic steps.

Velocity structure

The velocity structure of free-surface flow over a cyclic step morphology is anomalous with respect to regular open-channel flow. Hydraulic jumps formed at the start of the stoss-side of cyclic steps are able to drastically decrease flow velocities, often developing multiple vortices and rollers displaying negative velocities, mostly (but not solely) at the top of the flow. The actual hydraulic jump, where Fr=1, is not always located exactly at the trough of a cyclic step. Sometimes the hydraulic jump forms well upstream of the trough at about 70% of the lee-side, measured from the crest to the trough. This corresponds with the observations of Cartigny et al. (2013). The highest flow velocities downstream of the hydraulic jump are generally located near the bed-fluid interface. The drag on top of a high-concentration "undercurrent" with the near-stationary water on top, is larger than the experienced at the bed. The flow only equilibrates towards a normal open-channel velocity structure when the crest of the cyclic step is reached. The higher velocities near the bottom-layer have consequences for the local shear-stresses. Local excess shear-stresses do not decrease rapidly but rather dampen out gradually at the hydraulic jump because the near-bed layer keeps exerting shear-stress on the bed. The dense undercurrent below the hydraulic jump may still be experiencing a gravitational pull due to the slope of the lee-side as the hydraulic jump often is not located at the trough of the bedform, at the same time, a drag both at the bed interface and at the vortex-undercurrent-interface slow the current down.

Flow regime

The transition from subcritical to supercritical flow does not seem to align with the top of the crest. According to the time-series data the mean Froude number at a crest is 1.22 (σ=0.15, n=29). In open channel hydraulics it is generally assumed that the flow over a weir is critical, according to this data the flow becomes critical just before the "weir-type" crest. It should be mentioned however that the Froude number increases very rapidly at this region of the flow, and Froude numbers at unity are found very close to the crest as well. It is unlikely this observation is a statistical artefact because the samples in the time-series are taken with a 2-second interval, and one would expect both overestimations and underestimations from the true crestal Froude number to deviate around the mean, which they do, and none of the measurements display subcritical flow. Parker & Izumi (2000), Fagerazzi & Sun (2004), Sun & Parker (2005) and Balmforth & Vakil (2012), suggest lee-side of a cyclic step is defined by supercritical flow and the stoss-side by subcritical flow. There are two things that could explain the different outcomes of this study and the depth-averaged simulations: (1) subcritical and supercritical flow do not exactly coincide with deposition and erosion thresholds, allowing critical flow not to be located at the crest and the hydraulic jump to be located not exactly at the trough of a cyclic step, or (2) although the system may be in macroscopic equilibrium, the observed cyclic steps in the simulation are not in full equilibrium yet. It is observed that the undefined supercritical bedforms migrate upstream and increase in wavelength upstream, the wavelength may not have reached an equilibrium value yet, and Froude numbers larger than unity (indicative of erosion according to Parker & Izumi (2000), Fagerazzi & Sun (2004), Sun & Parker (2005) and Balmforth & Vakil (2012)) at the crest could elongate the cyclic step to reach a stable wavelength.

Another interesting observation associated with the hydraulic jumps is that according to the hydraulic jumps classification of Ven Te Chow (1973) (table 1), one would expect undular or weak hydraulic jumps as incoming Froude numbers (Fr_{90}) are <2.5. The observed hydraulic jumps however

do no show such a weak character and appear to closer resemble an oscillating or steady jump. The cause of this may be that either the angle of incoming flow results in different behaviour of the hydraulic jump, or the suspended sediment causes the flow to behave different resulting in another type of hydraulic jump.

Shear stresses

The observed median excess shear stress increases gradually with an increase in flow velocity, excess shear stresses also decrease gradually with suddenly decreasing depth-averaged flow velocities. Please note again that the term "excess shear stress" is used as defined in the results section in order to keep consistency with the numerical code. The median excess shear stress of the supercritical flow is higher than that of the subcritical flow. The high-stress pulses as observed in figure 23 are in the order of 5 times larger than the average stress in the supercritical flow, and are based upon one single point which interpolated from, the possibility that these points are numerical artefacts thus has to be kept in mind. For this reason the median excess shear stress is taken into account rather than the mean; to filter out these peaks.

The gradual decrease of excess shear stress is an effect of (1) the lack of high shear stress intervals in the subcritical regime which does not start simultaneously at every cyclic step and (2) at the hydraulic jump, the dense undercurrent is able to maintain its momentum for a relatively long period of time, still able to exert shear-stresses on the bed. Shear stresses are a dominant force in both bringing sediment in suspension for entrainment, and in bed-load transport, via the Shields equation 3.5 and 3.6, and equations 3.8 and 3.9 quantifying suspended and bed-load transport, respectively.

Sediment concentration

The amount of sediment in suspension is a function of the advection, settlement and entrainment of sediment. The velocity-field is dominant in the equations 3.1 through 3.4 governing the fall-out of sediment , shear stresses however are responsible for the entrainment of the sediment, either via the suspended or bed-load (equations 3.5 through 3.9), velocity (indirectly) also plays an important role here. The response of the sediment on the velocity field is that the amount of sediment in suspension almost doubles from 6-8 kg/m² as the flow goes over the crest of a cyclic step, to 12-14kg/m² in the supercritical flow regime as the hydraulic jump is reached. The sediment does not fall out of suspension immediately after the hydraulic jump; the average hydraulic jump is located at 500 (normalized time units), the amount of sediment in suspension only starts to drop 250 normalized time units later (~25-30 seconds). Figures 24 and 25 verify this lag of sediment fall-out. The sediment concentrations near the bed are clearly highest after the hydraulic jump occurred (at ~30 seconds or ½m later). The amount of sediment which falls out of suspension reduces to about 7 kg/m² again as the next crest is reached.

Depositional pattern

Overall there is net-deposition on the stoss-side of the cyclic step. The shear stresses remain relatively high for the first third of the stoss-side of a cyclic step, within the subcritical region just after the hydraulic jump, in combination with the required settling time of sediment, this results in a lag time and limited deposition. In the downstream two-thirds of a cyclic step, near-bed flow velocities are lower and most sediment falls out of suspension, creating backset lamination. In figure 22 the cumulative sediment mass corresponds with this pattern, between 500 and 750 normalized time units there is almost no sediment fall-out, after 750 time-units the suspended sediment mass drops with a roughly uniform slope, requiring a uniform thickness in deposits. The backset laminations are cross-cut by a downstream-dipping, upstream migrating scour surface created by the overall supercritical flow on the lee-side of a cyclic step.

This internal character does not entirely correspond with the internal structures as observed by Cartigny et al. (2013) (figure 1), displaying thicker deposits near the hydraulic jump decreasing in dip downstream. This difference in internal structure could be result of the mono-disparity of the simulated system; there is no variance in critical shear stress of different grains so most deposits in the simulated flow will accumulate where flow velocities near the bed are lowest. Whenever a more normal grain-size distribution - or even coarse tail - is used, those sediments will deposit earlier on. The upstream dipping laminations show a similar geometry to the upstream part of hydraulic jump bars as described in MacDonald et al. (2009), similar processes are at play, but in the case of cyclic steps, subcritical flow erodes downstream-areas and prevents the described cross-sets from forming.

Flow-dynamics and bed-interaction in turbidity currents

The flow characteristics of turbidity currents are different than those of free-surface flows, this may also affect their bed interaction as seen in the results. The behaviour of supercritical-flow turbidity currents is discussed here.

Velocity structure and flow-regimes

The flow-structure of a turbidity current is different from that of a free-surface flow. Highest flow velocities are found near the bed-layer as the drag on top of the current – due to the ambient water – is larger than the drag along the bed. A typical turbidity current velocity profile is seen in the simulated current up until a hydraulic jump occurs. The hydraulic jump is defined by analysis of the Froude numbers, via equation 1.4, an arbitrary cut-off-value for the top of the flow (0.05 m/s) is used for the depth-averaging method. The integral method as described in Garcia & Parker (1993) provided Froude numbers not prone to arbitrary cut-off values, and the numbers are mostly similar. It is only at the hydraulic jump that the values of the integral method deviate strongly from that of the depth-averaging method. This discrepancy between the methods is caused by a flaw in the straightforward application of the integral method of Garcia & Parker (1993), which is unable to deal correctly with negative velocities in the x-direction observed at the roller. Garcia & Parker (1993)'s second equation (12b therein) squares the velocity; when negative x-velocities are squared they become positive and will this lead to a strong overestimation of the velocity, resulting in an overestimation of the Froude number. This is what can be seen in figure 29. In this case the depth-averaging method for calculation of the Froude number would be more correct, even though an arbitrary cut-off value is used. The equations as posed in Garcia & Parker (1993) could be manipulated to correct for the overestimation of velocities at hydraulic jumps; by not simply squaring the x-velocities, but multiplying the velocities by an absolute value of themselves.

Shear stresses

Nonetheless it is clear a hydraulic jump is present which has developed a clear high-density roller below a lower-density detached flow. The effect of the velocity structure on the local excess shear stresses are significant. Before and after the hydraulic jump a normal velocity profile is seen, resulting in a character in which excess shear stresses are observed before (and after) the hydraulic jump, generally between 1-5 but peak excess shear stresses reach up to 15, and no excess shear stresses (at all) at the inverted velocity profile observed at the hydraulic jump. Just as in the free-surface flows, surges of peak (3-4 times average) excess shear stress can be observed.

Sediment concentration

The effect of the velocity and excess shear-stress distribution on the sediment concentrations in the flow is profound. As expected a dense near-bed layer is seen before the hydraulic jump figure 32 suggests the flow is slightly depositional at first (as reflected by the deposits in figure 33). At the hydraulic jump the Froude number drops to subcritical values, the flow velocity of the detached flow

however remains close to 1 m/s at a z-axis level of about 1m, interestingly enough this is about the same as before the hydraulic jump, even though the amount of suspended sediment in this part of the flow is very low. On profile 3 of figure 31 it can be seen that the amount of sediment in suspension at the 1m (on the z/elevation axis), is almost 0, the velocity is 1 m/s, this means all sediment has moved into the high-density (700-1200 kg/m³) roller. Two questions arise here: (1) why is the suspended sediment in the roller not deposited very quickly as no excess shear stresses are observed? And (2) how is it possible the flow on top of this roller is able to have a velocity of 1 m/s whilst is has almost no excess density anymore?

The first question probably has to do with the water in between the grains unable escape fast enough and thus preventing compaction up to the critical packing fraction and hindered settling, this means a high-density suspended sediment cloud remains. The second question posed does not have such a straightforward explanation. Whenever sediment is entrained by a flow, energy is required to bring the sediment into motion; this will slow down the flow as a result; conservation of energy and momentum. In the model, the inverse of this is happening as well; the Navier-Stokes equations governing the FLOW-3D® model describe conservation of momentum, energy and mass. As sediment is settled down, the kinetic energy in the sediment grains, however, is not dissipated by the impact on the bed (via heat or motion) as would be expected in the real world. The laws of conservation however still apply and the kinetic energy in the grains is transferred to the (fluid) flow, accelerating it as a result. This is probably what is happening at the hydraulic jump here as well; a large amount of sediment rapidly falls out of suspension, accelerating the flow overlying the high-concentration roller as a result. Part of the sediment then is deposited on the bed, another fraction is entrained again at the end of the roller creating an excess-density-driven turbidity current once again. The physics of the model here may not actually reflect the processes as they occur in the physical world completely. An exact in-depth analysis of this process in the model exceeds the scope of this study, it is however important to keep in mind that the physics in the model may not accurately mimic nature which makes the validity of the model around the submerged hydraulic jump questionable.

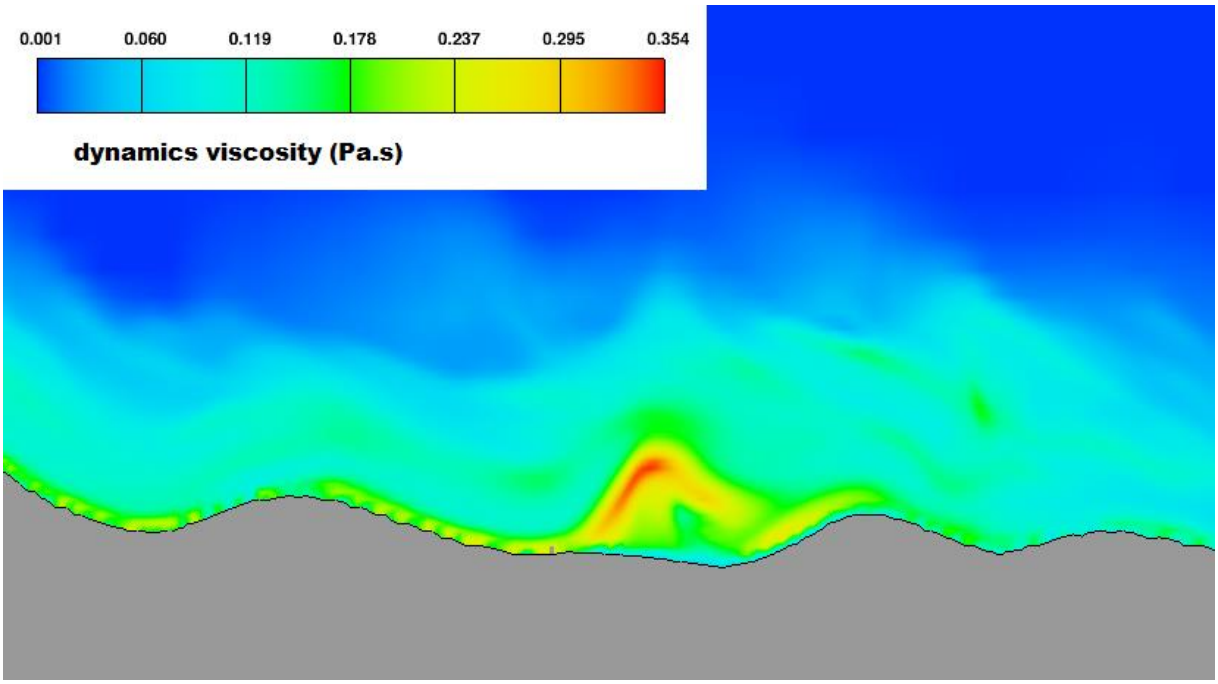

Figure 35: the dynamic (or apparent) viscosity in the modelled turbidity current

Depositional pattern

The amount of deposited sand after the hydraulic jump is significantly higher than before the hydraulic jump (figure 33), not only at the hydraulic jump and subcritical flow itself but also in the subsequent supercritical flow, this high deposition rate corresponds with the decrease in sediment mass in suspension after the hydraulic jump. The stratification in the flow however seems to be stronger than observed in the flow (i.e. higher densities in the near-bed layer). A reduced turbulence may be a cause for this, figure 34 shows that the dynamic viscosity (a result of turbulence, see equations 2.1 to 2.7) is much less after the hydraulic jump (generally <0.1 Pa.s near the bed) than before it (~0.2 Pa.s near the bed). Overall the simulated system is depositional, but it is clear that the supercritical flow before the hydraulic jump is much less depositional than the flow at the hydraulic jump, or the (supercritical) flow after it. There is a tendency of the bedforms to migrate upstream as the deposits on the stoss-side do exceed that of on the lee-side (figure 33). The bedform directly after the hydraulic jump shows backset lamination, similar to that on the stoss-side of a cyclic step, the loss of shear stress on the bed at the hydraulic jump creates a hummock as seen in figure 33. The facies attributed to hydraulic jumps in turbidity currents typically show scour (flames) at the begin of a hydraulic jump followed by rapid settling of sediments (typically upstream dipping and coarse-tail graded) just after the hydraulic jump (Postma et al., 2009; Postma et al., *in press*). Rapid settling after the hydraulic jump has been observed in the simulation. The structure is not only upstream dipping but includes a hummock-like morphology. A clear scour character directly at the hydraulic jump is not seen however, possibly because the system created is too depositional. Grain-size effects are not simulated as a mono-disperse sediment mixture is used.

Conclusions

Depth-resolved RANS numerical models are capable of simulating cyclic steps in an open-channel setting, and correct rates of sediment transport, resulting in migration of these bedforms. Flow properties and bed geometries as observed in the numerical simulations display a high degree of similarity to the cyclic steps described in literature. Other supercritical-flow bedforms; antidunes, breaking antidunes and chutes-and-pools, have not been simulated correctly at flow conditions at which they were observed to be formed in experimental settings. The bedforms observed in the simulations do not fit in any of the supercritical-flow bedform categories. It could either be that the classical be supercritical-flow bedform stability diagram is not completely accurate and more transitional-type bedforms exist, or the model is unable to capture the dynamics of the other supercritical-flow bedforms.

The ratio between $Froude_{50}$ and $Froude_{90}$ appears to provide an excellent indication of when cyclic step-morphology is present ($Fr_{90}/Fr_{50}>1.6$), though the ratio is probably a result of the morphology, not a governing factor, which the slope more likely is. The slope of the system is dependent on several factors. In general increased sediment discharge increases the equilibrium slope of the system, an increase in grain size has the same effect. Whenever cyclic steps are a more efficient way of transporting sediment in an overall supercritical flow, allowing lower mean slopes, cyclic steps will be formed, although the effects of other supercritical bedforms have not yet been taken into account.

The flow structure over an open-channel cyclic step displays an anomalous velocity structure with respect to typical open-channel flow. Just downstream of a hydraulic jump, highest flow velocities are found near the bed and lowest at the top of the flow, the effect of this remains observable over the entire stoss-side of a cyclic step. Over the predominantly supercritical lee-side the flow-structure is normal. The point of critical flow and hydraulic jump do not correspond with the crest and though

of the bedform exactly, either the assumption that supercritical flow is always erosional is wrong, or there is no true equilibrium on the bedforms yet. Median excess shear stresses at the lee-side of the cyclic step exceed that of the subcritical flow, the increase of excess shear stress corresponds with increasing depth-averaged flow velocities. The excess shear stress decreases gradually, even though depth-averaged flow-velocities decrease rapidly at a hydraulic jump, this is because highest flow velocities remain just above the bed. Most sediment is entrained on the lee-side, causing it to be erosional, the high near-bed velocities at the upstream part of the subcritical region however still induce shear stresses on the bed to such a degree that sediment mainly starts to settle at the downstream two-thirds of a cyclic step subcritical region, which roughly corresponds with the stoss-side. The interplay between deposition at the downstream two-thirds of the stoss-side, and erosion at the lee-side, creates backset, upstream dipping laminations that are cross-cut by an upstream-migrating, downstream-dipping erosional surface, which also causes upstream migration of the bedforms.

The simulated supercritical turbidity current shows a classical turbidity current flow structure for the most part but an anomalous velocity structure at the observed hydraulic jump. Bed shear stresses are highest in the supercritical flow and near-zero below the hydraulic jump, where a high-density roller is developed, overlain by low-density detached flow. Sediment in suspension is mainly located near the bed in the supercritical flow, but at the hydraulic jump there is a lack of sediment in the high-velocity detached flow, most of the sediment is suspended within the roller. The model may not accurately dissipate energy of deposited sediment and produces an acceleration of the fluid to conserve energy and momentum, this could explain high velocities observed over the hydraulic jump roller, and the validity of the model in this region can thus be questioned. The system is overall depositional and slight upstream migration of bedforms showing backset lamination is observed, a distinct hummock of sediment is deposited at the hydraulic jump.

Acknowledgements

I would like to thank Matthieu Cartigny and Joris Eggenhuisen for supervising me during this thesis and their fruitful and constructive comments and discussions. Ernst Hansen, Romain Rouzairol, Evgeniy Tanserev, and other staff at of Complex Flow Design AS are gratefully thanked for allowing me to use their numerical modelling code and hardware and, for sharing their modelling knowledge and experience with me. FlowScience Inc. and George Wei are thanked for developing and continuously improving the numerical code.

References

Alexander, J., Bridge, J. S., Cheel, R. J., & Leclair, S. F. (2001). Bedforms and associated sedimentary structures formed under supercritical water flows over aggrading sand beds. Sedimentology, 48(1), 133-152.

Ayranci, K., Lintern, D. G., Hill, P. R., & Dashtgard, S. E. (2012). Tide-supported gravity flows on the upper delta front, Fraser River delta, Canada. Marine Geology, 326, 166-170.

Basani, R., Janocko, M., Cartigny, M.J.B., Hansen, E.W.M., Eggenhuisen, J.T., (*in press*) MassFLOW-3D^{TM} as a simulation tool for turbidity currents: some preliminary results

Cartigy, M.J.B. (2012) Morphodynamics of supercritical high-density turbidity currents (PhD Thesis Utrecht University).

Cartigny, M. J. B., Ventra, D., Postma, G., & Van den Berg, J. H. (2013). Morphodynamics and sedimentary structures of bedforms under supercritical-flow conditions: new insights from flume experiments. *Sedimentology,* DOI: 10.1111/sed.12076 .

Chanson, H. (1999, January). Boundary Shear Stress Measurements below Free-Surface Standing Waves: Application to Bed Form Processes. In 28th IAHR Congress.

Chanson, H. (2000). Boundary shear stress measurements in undular flows: Application to standing wave bed forms. Water Resources Research, 36(10), 3063-3076.

Clarke, J. H., Brucker, S., Muggah, J., Hamilton, T., Cartwright, D., Church, I., & Kuus, P. (2012). Temporal progression and spatial extent of mass wasting events on the Squamish prodelta slope.

Covault, J. A., Kostic, S., Paull, C. K., Ryan, H. F., & Fildani, A. (*in press*). Submarine Channel Initiation, Filling And Maintenance From Seafloor Geomorphology And Morphodynamic Modelling Of Cyclic Steps. Sedimentology.

Duller, R. A., Mountney, N. P., Russell, A. J., & Cassidy, N. C. (2008). Architectural analysis of a volcaniclastic jökulhlaup deposit, southern Iceland: sedimentary evidence for supercritical flow. Sedimentology, 55(4), 939-964.

Fagherazzi, S., & Sun, T. (2003). Numerical simulations of transportational cyclic steps. Computers & geosciences, 29(9), 1143-1154.

Garcia, M., & Parker, G. (1993). Experiments on the entrainment of sediment into suspension by a dense bottom current. Journal of Geophysical Research: Oceans (1978–2012), 98(C3), 4793-4807.

Grant, G. E. (1997). Critical flow constrains flow hydraulics in mobile-bed streams: A new hypothesis. Water Resources Research, 33(2), 349-358.

Fielding, C. R. (2006). Upper flow regime sheets, lenses and scour fills: Extending the range of architectural elements for fluvial sediment bodies. Sedimentary Geology, 190(1), 227-240.

Fildani, A., Normark, W. R., Kostic, S., & Parker, G. (2006). Channel formation by flow stripping: Large-scale scour features along the Monterey East Channel and their relation to sediment waves. Sedimentology, 53(6), 1265-1287.

Gilbert, G. K.(1914) The transportation of debris by running water. U.S. Geol. Surv. Prof. Pap., 86, 263 pp

Grant, G. E. (1997). Critical flow constrains flow hydraulics in mobile-bed streams: A new hypothesis. Water Resources Research, 33(2), 349-358.

Guy, H. P., Simons, D. B.and Richardson, E. V. (1966) Summary of alluvial channel data from flume experiments 1956–1961. U.S. Geol. Surv. Prof. Paper,461-1..

Gou, J. (2002). Hunter Rouse and Shields Diagram., pg 1096-1098. World Scientific, Singapore, 2002.

Hager, W. H. (1992). Energy dissipators and hydraulic jump (Vol. 8). Springer.

Heiniö, P., & Davies, R. J. (2009). Trails of depressions and sediment waves along submarine channels on the continental margin of Espirito Santo Basin, Brazil. Geological Society of America Bulletin, 121(5-6), 698-711.

Jorritsma, 1973. Onderzoek naar de taluthellingen van onder water aangebracht zand. Waterloopkunding laboratorium: verslag modelonderzoek. M1118, augustus 1973. (in Dutch).

Kennedy, J.F. (1960) Stationary Waves and Antidunes in Alluvial Channels. PhD Thesis. California Institute of Technology.

Kennedy, J.F. (1961) Stationary Waves and Antidunes in Alluvial Channels. W.M. Keck Laboratory of Hydraulics and Water Research, California Institute of Technology, Report KH-R-2, 146pp.

Kostic, S., & Parker, G. (2006). The response of turbidity currents to a canyon–fan transition: internal hydraulic jumps and depositional signatures. *Journal of Hydraulic Research*, *44*(5), 631-653.

Kostic, S., Sequeiros, O., Spinewine, B., & Parker, G. (2010). Cyclic steps: A phenomenon of supercritical shallow flow from the high mountains to the bottom of the ocean. Journal of Hydro-environment Research, 3(4), 167-172.

Lamb, M. P., Parsons, J. D., Mullenbach, B. L., Finlayson, D. P., Orange, D. L., & Nittrouer, C. A. (2008). Evidence for superelevation, channel incision, and formation of cyclic steps by turbidity currents in Eel Canyon, California. Geological Society of America Bulletin, 120(3-4), 463-475.

Lee, M., Malaya, N., & Moser, R. D. (2013, November). Petascale direct numerical simulation of turbulent channel flow on up to 786k cores. In Proceedings of SC13: International Conference for High Performance Computing, Networking, Storage and Analysis (p. 61). ACM.

Long, D. , Steffler, P. M. and Rajaratnam, N.(1990) 'LDA study of flow structure in submerged hydraulic jump', Journal of Hydraulic Research, 28: 4, 437 — 460

MacDonald, R. G., Alexander, J., Bacon, J. C., & Cooker, M. J. (2009). Flow patterns, sedimentation and deposit architecture under a hydraulic jump on a non-eroding bed: defining hydraulic-jump unit bars. Sedimentology, 56(5), 1346-1367.

Mastbergen, D.R.and Winterwerp, J.C.(1987) Het gedrag van zand-watermengselstromingen boven water: Verslag experimentele vervolg studie. Report Z46-02, Delft Hydraulics, Delft, The Netherlands

Mastbergen, D. R., & Van Den Berg, J. H. (2003). Breaching in fine sands and the generation of sustained turbidity currents in submarine canyons. Sedimentology, 50(4), 625-637.

Orton, G. J., & Reading, H. G. (1993). Variability of deltaic processes in terms of sediment supply, with particular emphasis on grain size. Sedimentology, 40(3), 475-512.

Parker, G. (1996). Some speculations on the relation between channel morphology and channel-scale flow structures. Coherent flow structures in open channels, 423.

Parker, G., & Izumi, N. (2000). Purely erosional cyclic and solitary steps created by flow over a cohesive bed. Journal of Fluid Mechanics, 419, 203-238.

Paull, C. K., Caress, D. W., Ussler, W., Lundsten, E., & Meiner-Johnson, M. (2011). High-resolution bathymetry of the axial channels within Monterey and Soquel submarine canyons, offshore central California. *Geosphere*, *7*(5), 1077-1101.

Pettingill, H. S., & Weimer, P. (2002). Worlwide deepwater exploration and production: Past, present, and future. The Leading Edge, 21(4), 371-376.

Postma, G., Cartigny, M., & Kleverlaan, K. (2009). Structureless, coarse-tail graded Bouma Ta formed by internal hydraulic jump of the turbidity current?. Sedimentary Geology, 219(1), 1-6.

Postma, G., Cartigny, M., & Kleverlaan, K. (in press). Recognition of cyclic steps in sandy and gravelly turbidite sequences and consequences for the Bouma facies model.

Rodi. W. Turbulence models and their application in hydraulics: a state of the art review. International Association for Hydraulic Research (IAHR), Delft, The Netherlands, 1980.

Sabbagh-Yazdi, S., Rostami, F. and Mastorakis, N. (2007) Turbulent modeling effects on finite volume solution of three dimensional aerated hydraulic jumps using volume of fluid, pp. 168-174. World Scientific and Engineering Academy and Society (WSEAS).

Smith, D. P., Kvitek, R., Iampietro, P. J., & Wong, K. (2007). Twenty-nine months of geomorphic change in upper Monterey Canyon (2002–2005). *Marine Geology*, *236*(1), 79-94.

Spinewine, B., Sequeiros, O. E., Garcia, M. H., Beaubouef, R. T., Sun, T., Savoye, B., & Parker, G. (2009). Experiments on wedge-shaped deep sea sedimentary deposits in minibasins and/or on channel levees emplaced by turbidity currents. Part II. Morphodynamic evolution of the wedge and of the associated bedforms. Journal of Sedimentary Research, 79(8), 608-628.

Sun, T., & Parker, G. (2005). Transportational cyclic steps created by flow over an erodible bed. Part 2. Theory and numerical simulation. Journal of Hydraulic Research, 43(5), 502-514.

Taki, K., & Parker, G. (2005). Transportational cyclic steps created by flow over an erodible bed. Part 1. Experiments. Journal of Hydraulic Research, 43(5), 488-501.

Tuan, L.A. (2011) Open Channel Hydraulics for Engineers. Saarbrücken. LAP Lambert Academic Publishing.

Winterwerp, J. C., Bakker, W. T., Mastbergen, D. R., & van Rossum, H. (1992). Hyperconcentrated sand-water mixture flows over erodible bed. Journal of Hydraulic Engineering, 118(11), 1508-1525.

Wong, M., & Parker, G. (2006). Reanalysis and correction of bed-load relation of Meyer-Peter and Müller using their own database. Journal of Hydraulic Engineering, 132(11), 1159-1168.

Appendix 1: data all free-surface simulations

Simulation	Conc. kg/m³	Spec. Dis. m²/s	Grainsize um	bedform	u50 m/s	u90 m/s	Fr50 -	Fr90 -	h50 m	migr. Freq /s	migr. Freq. /s	migr. period s	migr. period s	timespan s	slope deg
f1_1	150	0.093	350	1	1.07	1.7	1.15	2.3	0.1	0.00843		118.623962		200-1800	2.4
f1_2	150	0.093	350	6	1.26	1.67	1.48	2.2	0.09	0.0075	0.016-0.027	133.3333333	30-60	200-1800	1.5
f1_3	150	0.093	350	6	1.3	1.65	1.5	2.1	0.09	0.0085		117.6470588		200-1800	1.1
f2_1	150	0.077	350	1	0.97	1.64	1.08	2.4	0.09	0.0085		117.6470588		200-1800	2.2
f2_2	150	0.077	350	6	1.2	1.52	1.44	2.14	0.08	0.0085	0.015-0.004	117.6470588	30-100	200-1800	1.4
f2_3	150	0.077	350	6	1.16	1.45	1.4	2	0.08	0.0085		117.6470588		200-1800	0.8
f3_1	75	0.093	350	1	1.15	1.61	1.3	2.14	0.09	0.0085		117.6470588		200-1800	1.4
f3_2	75	0.093	350	6	1.27	1.54	1.44	1.96	0.09	0.0075		133.3333333		200-1800	1.05
f3_3	75	0.093	350	6	1.21	1.48	1.38	1.86	0.09	0.0075		133.3333333		200-1800	0.5
f4_1	150	0.12	350	1	1.09	1.71	1.02	1.99	0.12	0.0085	0.0038	117.6470588	263.1578947	200-1800	2
f4_2	150	0.12	350	6	1.39	1.89	1.5	2.37	0.11	0.0075		133.3333333		200-1800	1.6
f4_3	150	0.12	350	6	1.39	1.82	1.48	2.2	0.11	0.0075		133.3333333		200-1800	0.9
f5_1	175	0.093	350	1	0.96	1.7	0.93	2.29	0.11	0.0075		133.3333333		200-1800	2.2
f5_2	175	0.093	350	6	1.32	1.7	1.51	2.26	0.09	0.0075		133.3333333		200-1800	1.7
f5_3	175	0.093	350	6	1.33	1.65	1.59	2.2	0.09	0.0075		133.3333333		200-1800	1.4
f6_1	150	0.05	350	1	1.01	2.48	1.44	2.5	0.04	0.0093		107.5268817		200-1800	2.2
f6_2	150	0.05	350	6	0.97	1.19	1.34	1.83	0.06	0.0085		117.6470588		200-1800	0.4
f6_3	150	0.05	350	5	0.75	0.91	0.89	1.2	0.07	0		0		200-1800	0.15
f7_1	150	0.093	160	5	0.46	0.64	0.29	0.42	0.26			0		200-1800	0
f7_2	150	0.093	160	5	0.86	1	0.8	0.97	0.11	0.0065		153.8461538		200-1800	0
f7_3	150	0.093	160	5	0.8	0.91	0.75	0.84	0.12	0		0		200-1800	0
f8_1	150	0.093	265	1	1	1.53	1	1.93	0.1	0.0085		117.6470588		200-1800	2.1
f8_2	150	0.093	265	6	1.23	1.56	1.38	1.98	0.09	0.0085	0.0052	117.6470588	192.3076923	200-1800	1.8
f8_3	150	0.093	265	6	1.19	1.64	1.36	2.12	0.095	0.0085	0.0056	117.6470588	178.5714286	200-1800	1.3
f9_1	150	0.093	450	1	1.33	1.8	1.6	2.52	0.09	0.0075		133.3333333		200-1800	2.7
f9_2	150	0.093	450	6	1.35	1.68	1.56	2.2	0.09	0.0065		153.8461538		200-1800	2
f9_3	150	0.093	450	6	1.3	1.6	1.47	2	0.09	0.0065		153.8461538		200-1800	1.5
f11_1	150	0.077	265	1	0.96	1.5	1.07	2.07	0.09	0.0056	0.011	178.5714286	90.90909091	200-1800	2.2
f11_2	150	0.077	265		1.06	1.52	1.21	2.12	0.09	0.0094		106.3829787		200-1800	1.5
f11_3	150	0.077	265		1.11	1.51	1.33	2.1	0.08	0.0094		106.3829787		200-1800	1
f12_1	150	0.05	265	1	0.94	1.35	1.3	2.18	0.06	0.0103		97.08737864		200-1800	1.4
f12_2	150	0.05	265	6	0.92	1.2	1.22	1.84	0.06	0.0094	0.0019	106.3829787	526.3157895	200-1800	0.9
f12_3	150	0.05	265	6	0.9	1.15	1.18	1.78	0.06	0.012		83.33333333		200-1800	0.2
f14_1	150	0.16	265	2	1.13	1.36	0.91	1.2	0.1336	0.0075		133.3333333		400-1800	1.5
f14_2	150	0.16	265	2	1.14	1.93	1.17	2.11	0.144	0.00937		106.7235859		200-1800	1.2
f14_3	150	0.16	265	2	1.41	1.88	1.31	2	1.334	0.004689	0.0075	213.2650885	133.3333333	200-1800	0.8

Appendix 2: Free-surface flow analysis


```
clear all
close all
```

load wanted data

data format should be: column1=time [s] column2=sediment height [m] column3=free-surface height [m] column4=Froude number [-] column5=depth averaged velocity [m/s]

```
load('f2_2_2m.txt')
input=f2_2_2m;                              %change name to file name minus extension
t0=101;
tend=901;

%load and select data for slope calculation
load('f2_2_8m.txt')
shmax=f2_2_8m(t0:tend,2);
load('f2_2_11m.txt')
shmin=f2_2_11m(t0:tend,2);

%flow data at 8m
t=input(t0:tend,1);
sh=input(t0:tend,2);
fs=input(t0:tend,3);
fr=input(t0:tend,5);
u=input(t0:tend,4);
g=9.81;
```

Froude number

```
plot(t,fr)                  %show all Fr over time
sortfr=sort(fr);            %sort Froude numbers
plot(sortfr,'.')
hold on

num50=round(length(sortfr)*0.5);            %find element no. Fr50
num90=round(length(sortfr)*0.9);            %find element no. Fr90
fr50=sortfr(num50);                         %corresponding Fr no.
fr90=sortfr(num90);                         %corresponding Fr no.

plot(num50,fr50,'or')
plot(num90,fr90,'or')
xlabel('number of measurements [-]')
ylabel('Froude number [-]')
text(num50-35,fr50,'Froude50\rightarrow')
text(num90-35,fr90,'Froude90\rightarrow')
```

```
figure
subplot(3,1,1)
plot(t,fr,'k')                      %calculated Froude
hold on
xlabel('time [s]')
ylabel('Froude number [m]')
```

sediment height and period of waveforms

```
hold off

shsmooth=smooth(sh,20);             %smoothened bed surface
[peak,loc]=findpeaks(shsmooth);     %find peaks [sedheigh, elementno.]
tpeak=t(loc);                       %link element no. peak to time

for i=1:length(peak)-1              %if peaks are within 30seconds
       if tpeak(i+1)-tpeak(i)<15    %pick the highest one
            if peak(i+1)>peak(i)    %other is set to nan
               peak(i)=nan;
               tpeak(i)=nan;
            else
                peak(i+1)=nan;
                tpeak(i+1)=nan;
            end
       end
end
peak=peak(~isnan(peak));            %remove nan from array
tpeak=tpeak(~isnan(tpeak));

for i=2:length(tpeak)
   dtpeak(i)=tpeak(i)-tpeak(i-1);   %time difference between peaks
end
avgdtpeak=mean(dtpeak);             %average dt peak = avg period
h=fs-sh;                            %flow depth
havg=mean(h);                       %mean flow depth
%h10
sorth=sort(h);
numh10=round(length(sorth)*0.1);
numh50=round(length(sorth)*0.5);
h10=sorth(numh10);
h50=sorth(numh50);

subplot(3,1,2),
plot(t,sh,'k',t,fs,'b')
hold on
plot(t,shsmooth,'r',tpeak,peak,'or')
xlabel('time [s]')
ylabel('bed + free surf. height [m]')
```

flow velocity

```
sortu=sort(u);
```

```
unum50=round(length(sortu)*0.5);            %find element no. u50
unum90=round(length(sortu)*0.9);            %find element no. u90
u50=sortu(unum50);
u90=sortu(unum90);

subplot(3,1,3)
plot(t,u,'k')
xlabel('time [s]')
ylabel('depth averaged velocity [m/s]')
hold on
```

mobility parameters

```
%define constants
rho=1000;
rhos=2650;
d50=350e-6;
d90=350e-6;
%Chezy coefficient
c90=18*log10((4*h10)/d90);
%grain mobility parameter (Van den Berg & Van Gelder, 1993)
theta90=(rho*u90^2)/((rhos-rho)*c90^2*d50);
%grain shear stresses (Van Rijn, 1984)
tau90=9.81*rho*(u90^2/c90^2);
```

Froude numbers at crests

```
plot(t,shsmooth,'r',tpeak,peak,'or')
xlabel('time [s]')
ylabel('bed elevation [m]')
tpeak=round(tpeak);
for i=1:16
    frcrest(i)=fr(tpeak(i)/2);

end
frcr=frcrest(2:16);     %exclude first two
avgfrcr=mean(frcr);     %mean
stdvfrcf=std(frcr);     %standard deviation
```

average sediment height for slope calculation

```
meansh=mean(sh);

sortsh=sort(sh);

shnum50=round(length(sortsh)*0.5);

sh50=sortsh(shnum50);

% mean and sh50 are almost identical, so taking mean or median does not matter
avgshmax=mean(shmax);
avgshmin=mean(shmin);
tslp=(shmax-shmin)/10;
degtslp=tand(tslp);
```

```
figure
plot(t,tslp,'.')
xlabel('time [s]')
ylabel('slope [-]')

slp=(avgshmax-avgshmin)/(3);
deg=atand(slp);
% only keep relevant data
clearvars -except fr50 h10 h50 u50 u90 fr90 havg avgdtpeak u50 u90 input c90
theta90 tau90 slp
```

Published with MATLAB® R2013a

Appendix 3: subaqueous flow data analysis

- load data and create new vectors
- find peaks

load data and create new vectors

```
clear all
close all

tic
xlsread('lotsofvars8_xls.xlsx');
a=ans;

bx=a(:,1);                %x
by=a(:,2);                %y
bz=a(:,3);                %z
bp=a(:,4);                %pressure
bmu=a(:,5);               %dynamic viscosity
btke=a(:,6);              %turbulent energy
bc=a(:,7);            %suspended sediment concentration
bsh=a(:,8);               %packed sediment height
bfs=a(:,9);               %free surface height
bovel=a(:,10);            %velocity at bedinterface
bu=a(:,11);               %x velocity
btau=a(:,12);             %excess shear stress

% x-value
x{1}=bx(3:40);
x{2}=bx(46:83);

%y-value
z{1}=bz(3:40);
z{2}=bz(46:83);
%turbulent energy in J/kg
tke{1}=btke(3:40);
tke{2}=btke(46:83);
%sediment in suspention in kg/m³
c{1}=bc(3:40);
c{2}=bc(46:83);
%excess shear stress in [-]
tau{1}=btau(3:40);
tau{2}=btau(46:83);
%sediment height in m
sh{1}=bsh(3:40);
sh{2}=bsh(46:83);
%dynamics viscoisty in Pa.s
mu{1}=bmu(3:40);
mu{2}=bmu(46:83);
%total pressure in Pa
p{1}=bp(3:40);
p{2}=bp(46:83);
%free-surface height in m
fs{1}=bfs(3:40);
fs{2}=bfs(46:83);
%x-velocity in m/s
u{1}=bu(3:40);
```

```
u{2}=bu(46:83);
%velcoity at bed-interface
ovel{1}=bovel(3:40);
ovel{2}=bovel(46:83);

for i=3:901
x{i}=bx((43*(i-1)+3):(43*i)-3);
z{i}=bz((43*(i-1)+3):(43*i)-3);
tke{i}=btke((43*(i-1)+3):(43*i)-3);
c{i}=bc((43*(i-1)+3):(43*i)-3);
tau{i}=btau((43*(i-1)+3):(43*i)-3);
sh{i}=bsh((43*(i-1)+3):(43*i)-3);
mu{i}=bmu((43*(i-1)+3):(43*i)-3);
u{i}=bu((43*(i-1)+3):(43*i)-3);
ovel{i}=bovel((43*(i-1)+3):(43*i)-3);
fs{i}=bfs((43*(i-1)+3):(43*i)-3);
p{i}=bp((43*(i-1)+3):(43*i)-3);
end

toc
b=[0 1];

% load data from time series
load('f1_8m.txt')
input=f1_8m;
t0=1;
tend=901;
t=0:2:1800;
%flow data at 8m
% t=input(t0:tend,1);
sh=input(t0:tend,2);
fs=input(t0:tend,3);
fr=input(t0:tend,5);        %Froude number
avgu=input(t0:tend,4);      %depth avg u
g=9.81;

%delete sed conc. under bed
for i=1:901
    for j=1:38
   if z{i}(j)<sh(i)
      c{i}(j)=0;
   end
    end
    fill(i)=fs(i)-sh(i);
end

%make non-uniform data suitable
for i=1:901
    tau2(i)=max(tau{i});
    intC(i)=sum(c{i}(:));
end
```

```
Elapsed time is 2.619440 seconds.
```

find peaks

```
sh2=smooth(sh,30);

[ps pt]=findpeaks(sh2);

pt2=t(pt(:));

plot(t,sh2,'.k')
hold on
plot(pt2,ps,'or')

for i=1:length(pt2)
if pt2(i)<200
    pt2(i)=nan;
    ps(i)=nan;
end
end
tpeak=pt2(~isnan(pt2));
speak=ps(~isnan(ps));

%cut sh and t vectors in 12 vecors all of 1 cyclic step wavelength
for i=1:length(tpeak)-1
   tz1{i}=t(tpeak(i)/2:tpeak(i+1)/2);
   sz1{i}=sh(tpeak(i)/2:tpeak(i+1)/2);
   tauz1{i}=tau2(tpeak(i)/2:tpeak(i+1)/2);
   cz1{i}=intC(tpeak(i)/2:tpeak(i+1)/2);
   frz1{i}=fr(tpeak(i)/2:tpeak(i+1)/2);
   fsz1{i}=fs(tpeak(i)/2:tpeak(i+1)/2);

   t0(i)=tz1{i}(1);
   tmax(i)=tz1{i}(length(tz1{i}));
   dt(i)=tmax(i)-t0(i);

   for j=1:length(tz1{i})
      tz2{i}(j)=(tz1{i}(j)-t0(i))/dt(i); %time as fraction (0 to 1) crest-to-crest
      tz3{i}(j)=round(tz2{i}(j)*1000);
      if tz3{i}(j)==0
          tz3{i}(j)=1;
      end

   end

tv1{i}=1:1000;                    %12 0-1000 vectors for t
sv1{i}=zeros(1000,0);             %12 empty vectors of 1000 length for sh
tauv1{i}=zeros(1000,0);
cv1{i}=zeros(1000,0);
frv1{i}=zeros(1000,0);
fsv1{i}=zeros(1000,0);
   for j=1:length(tz3{i})
        sv1{i}(tz3{i}(j))=sz1{i}(j);
        tauv1{i}(tz3{i}(j))=tauz1{i}(j);
        cv1{i}(tz3{i}(j))=cz1{i}(j);
        frv1{i}(tz3{i}(j))=frz1{i}(j);
        fsv1{i}(tz3{i}(j))=fsz1{i}(j);
```

```
    end
    sv2{i}=spline(tz3{i},sz1{i},tv1{i});
    tauv2{i}=spline(tz3{i},tauz1{i},tv1{i});
    cv2{i}=spline(tz3{i},cz1{i},tv1{i});
    frv2{i}=spline(tz3{i},frz1{i},tv1{i});
    fsv2{i}=spline(tz3{i},fsz1{i},tv1{i});

end

% values for 12 cyclic steps
% sediment height
figure
for i=1:20
plot(tv1{i},sv2{i})
hold on
xlabel('normalized time')
ylabel('sediment height')
end
%shear stress
figure
for i=7
    subplot(2,2,1:2)
plot(tv1{i},tauv2{i},'r','linewidth',2)
hold on
xlabel('normalized time','fontsize',13)
ylabel('excess shear stress (-)','fontsize',13)
% ylim([0 20])


end

% mean of those 12


for j=1:1000

sv3(j)=(sv2{1}(j)+sv2{2}(j)+sv2{3}(j)+sv2{4}(j)+sv2{5}(j)+sv2{6}(j)+sv2{7}(j)+sv2{8
}(j)+sv2{9}(j)+sv2{10}(j)+sv2{11}(j)+sv2{12}(j))/12;

tauv3(j)=(tauv2{1}(j)+tauv2{2}(j)+tauv2{3}(j)+tauv2{4}(j)+tauv2{5}(j)+tauv2{6}(j)+t
auv2{7}(j)+tauv2{8}(j)+tauv2{9}(j)+tauv2{10}(j)+tauv2{11}(j)+tauv2{12}(j))/12;

cv3(j)=(cv2{1}(j)+cv2{2}(j)+cv2{3}(j)+cv2{4}(j)+cv2{5}(j)+cv2{6}(j)+cv2{7}(j)+cv2{8
}(j)+cv2{9}(j)+cv2{10}(j)+cv2{11}(j)+cv2{12}(j))/12;

frv3(j)=(frv2{1}(j)+frv2{2}(j)+frv2{3}(j)+frv2{4}(j)+frv2{5}(j)+frv2{6}(j)+frv2{7}(
j)+frv2{8}(j)+frv2{9}(j)+frv2{10}(j)+frv2{11}(j)+frv2{12}(j))/12;

fsv3(j)=(fsv2{1}(j)+fsv2{2}(j)+fsv2{3}(j)+fsv2{4}(j)+fsv2{5}(j)+fsv2{6}(j)+fsv2{7}(
j)+fsv2{8}(j)+fsv2{9}(j)+fsv2{10}(j)+fsv2{11}(j)+fsv2{12}(j))/12;


end
```

```
for i=1:1000
       cv4(i)=cv3(i)*0.02;
end
```

Published with MATLAB® R2013a

Appendix 4: calculation of Froude numbers (subaqueous)

- calculate froude number depth averaged
- integral froude no. (Garcia & Parker 1993)

calculate froude number depth averaged

use a matrix with distance (or time) on the x-axis and flow properties C, U, etc. on the Y-axis. Umat, Cmat and Zmat (where Z defines height in Y respectively. Also have a vector or matrix to prepresent the X-axis (x in this example)

```
umat2=umat;

cmat2=cmat;

zmat2=zmat;

% if the X-velocity is smaller than 0.05 (but positive! to preven nan of
% roller-vortex, set as nan.
for i=1:240
    for j=1:66
   if umat2(j,i)<0.05 && umat2(j,i)>-0.01
       umat2(j,i)=nan;
       cmat2(j,i)=nan;
       zmat2(j,i)=nan;
   elseif zmat2(j,i)>1.1
       umat2(j,i)=nan;
       cmat2(j,i)=nan;
       zmat2(j,i)=nan;
   end

    end
end

%densimetric froude number according to kostic (2010)
% Frd=U/sqrt(RCgH)
g=9.81;
rhos=2650;
rhow=1000;
R=(rhos/rhow)-1;

% is flow height (H), it is the maximum z-value minus the minimum, valid is
% zmat2 alreay has velicity <0.05 set to nan.
%calculate depth avg. values for C, U
for i=1:240
uavg2(i)=nanmean(umat2(:,i));
cavg2(i)=nanmean(cmat2(:,i));
cavg3(i)=cavg2(i)/2650;
H(i)=max(zmat2(:,i))-min(zmat2(:,i));

% densimetric Froude number
frd(i)=uavg2(i)/(sqrt(R*cavg3(i)*g.*H(i)));
end
%smoothen signal
smoothfrd=smooth(frd);
%
```

```
% figure
% plot(x(1:240,:),frd,'k')
% xlabel('location x in (m)')
% ylabel('Densimetric Froude number')
%
% figure
% plot(x(1:240,:),smoothfrd,'r','linewidth',2)
% xlabel('location x in (m)','fontsize',14)
% ylabel(' Smoothened Densimetric Froude number','fontsize',14)
% hold on
```

integral froude no. (Garcia & Parker 1993)

```
for i=1:240
    %create square of Ux velocities and make C fractions of sediment
    %concentration, not kg/m³
    for j=1:66
    umatsq(j,i)=umat(j,i).^2;
    cmatf(j,i)=cmat(j,i)/2650;
    end

    % integrate over dz (cell size =0.02m)
Uh(i)=nansum(umat(:,i))*0.02;
U2h(i)=nansum(umatsq(:,i))*0.02;
UCh(i)=nansum(umat(:,i).*cmatf(:,i))*0.02;

U(i)=U2h(i)/Uh(i);
C(i)=UCh(i)/Uh(i);
h(i)=UCh(i)/(U(i)*C(i));

%densimetric froude number
Frdx(i)=U(i)/(sqrt(R*C(i)*g.*h(i)));

end

plot(x(1:240,:),Frdx,'k','linewidth',2)
sFrdx=smooth(Frdx); % smooth signal

plot(x(1:240,:),sFrdx,'k','linewidth',2)
hold on
plot(x(1:240,:),smoothfrd,'r','linewidth',2)
xlabel('location x in (m)','fontsize',14)
ylabel(' Smoothened Densimetric Froude number','fontsize',14)
legend('Integral Method Garcia & Parker (1993)','Depth-average method Kostic et al.
(2010)')
xlim([8.1783 14.4130])
```

Published with MATLAB® R2013a